PREPRINT

Non-ideal MHD growth of current interchange tearing modes at plasma edge and response to externally-imposed flow

Hideaki Miura*
National Institute for Fusion Science, Toki, Gifu 509-5292, JAPAN

Linjin Zheng, Wendell Horton
Institute for Fusion Studies, University of Texas at Austin, Texas 78712-0262, U.S.A

(Dated: April 17, 2023)

Abstract

Current Interchange Tearing Modes (CITM) have been proposed to explain an intermittent eruption of electric current toward a divertor at an edge region of a tokamak device. Extended magnetohydrodynamic (MHD) simulations combined with the Scrape-Off-Layer (SOL) diffusion model, which has been developed by the authors (Miura, Zheng, and Horton, Physics of Plasmas **24**(2017)), are carried out in order to study growth of a CITM under influences of two-fluid and gyro-viscous effects, or non-ideal MHD effects. Numerical simulations both with and without an externally-imposed azimuthal flow show that the growth of a CITM is observed for a relatively small flow velocity, and that a CITM can be a candidate mechanism for intermittent eruption of the current in a tokamak, whether the growth is under influences of non-ideal MHD effects or not. The growth can be suppressed when an externally-imposed azimuthal flow is sufficiently large to cause a finite radial displacement, because such a displacement prevents a transition from an interchange to a tearing mode that is the key process of a CITM. Furthermore, It is also found that a stripe pattern similar to so-called streamers is formed in the course of the CITM growth. The basic nature of this streamer-like structure is also presented.

---

* miura.hideaki@nifs.ac.jp

I. INTRODUCTION

Edge physics of magnetically confined fusion plasma continue to gather much interest because of their complexity and importance. Amongst many subjects of edge plasma physics, generation of the Edge Localized Mode (ELM) and a large heat load on a reactor wall or a divertor plate, caused by an ELM eruption during the H-mode operation, are recognized as important subjects for the ITER and next-generation tokamak devices[1–7]. In the context of these studies, a quiescent H-mode (QH-mode) has been reported as an ELM-free operation mode[5, 8, 9]. Current bursts in the Scrape-Off-Layer (SOL) during the ELM period suggest a transition from a pressure-driven or peeling-ballooning mode[11] to a tearing mode[10].

In order to explain this transition theoretically, Zheng and Furukawa have proposed the current interchange tearing mode (CITM) theory[12, 13]. At the edge region, there is a steep pressure gradient which causes pressure-driven instabilities. Furthermore, the plasma current in the core region is large, while the current outside the Last Closed Flux Surface (LCFS) is low, due to saturation by the divertor sheaths, leading to formation of a current jump across the LCFS. The current jump across LCFS can convert the peeling-ballooning mode to the tearing modes due to the current interchange effects. On this occasion, a magnetic field line reconnection, which occurs as a consequence of the excitation of tearing modes, can enhance the discharging of particles and heat from the pedestal to the SOL. Since the magnetic field lines outside the LCFS are open toward the divertor plates, the particles and energy are brought beyond the LCFS and released rapidly to the divertor plates. This also results in a SOL current jump, as observed during the ELM activities[10].

In our previous work we developed a numerical model, the SOL diffusivity model, to enforce a low-level current outside the LCFS[14]. Numerical simulations of a resistive MHD model combined with the SOL diffusivity model in the literature have shown that an interchange mode transits to a tearing mode, as has been considered in [12, 13]. Since the transition is the key process in the CITM theory, the numerical results indicate the growth of a CITM in the course of a time-evolution.

Although growth of a CITM has been shown already in Ref.[14], edge plasma motions consist of more complex physics than that are described by a resistive MHD model. For example, since the edge pedestal width is often comparable to the ion skin depth, two-fluid effects and ion Larmor radius effects (non-ideal MHD effects) should influence the growth

AIP Publishing Physics of Plasmas ACCEPTED MANUSCRIPT
This is the author's peer reviewed, accepted manuscript. However, the online version of record will be different from this version once it has been copyedited and typeset.
PLEASE CITE THIS ARTICLE AS DOI: 10.1063/5.0106785

of a CITM. In fact, edge plasma physics have been studied extensively by the use of extended MHD (XMHD), gyro-fluid, or gyro-kinetic models. (See Refs.[15]-[18] and references therein.) For this reason, we extend our earlier work based on a resistive MHD model, to a study based on an XMHD model which includes the non-ideal effects. The primary purpose of this paper is to investigate growth of a CITM under the non-ideal MHD effects.

From the point of view of a CITM as a transition from an interchange to a tearing mode, this mode is closely related with pressure-driven instability as the first stage of its growth. With respect to a study of an unstable pressure-driven mode under the non-ideal MHD effects, it has been shown that the effects can reduce the growth rate of the unstable modes but do not necessarily suppress the instability sufficiently[19–22]. Thus we pay attention to growth of a CITM, especially in its first stage, in light of these earlier works[19–22].

With respect to non-ideal MHD effects, we also need to pay attention to an influence of flow to a CITM. While the non-ideal MHD effects often induce dia-magnetic flow, the edge region is often exposed to a flow driven by other effects as well. For this reason, we study a response of a CITM to an externally-driven flow, as the secondary purpose of this paper. The generation of the dia-magnetic flow can include many interesting subjects, such as interactions between the flow and magnetic islands. For all that, the center of our interest exists in the growth of a CITM, not in the generation of the dia-magnetic flow. We focus on the rapid growth of a CITM rather than long-term behavior such as flow-island interactions.

Our concern in this paper is basic nature of the CITM itself although the original CITM theory was developed for ELM-related events. Since the CITM theory is quite simple and is constructed without a complex edge physics, we are interested in the robustness of the theory to physics which should be included in edge physics investigations. For this reason, we study growth of a CITM in the shear-slab configuration, not in a toroidal configuration, being apart from a realistic ELM-related subjects.

This paper is organized as follows. In §.2,outlines of numerical simulations are presented. Initial equilibrium for a CITM, governing equations, numerical models including the SOL diffusivity model developed in Ref.[14]. In §.3, simulation results are presented. In §.4, concluding remarks and discussions are presented.

AIP Publishing Physics of Plasmas ACCEPTED MANUSCRIPT
This is the author's peer reviewed, accepted manuscript. However, the online version of record will be different from this version once it has been copyedited and typeset.
PLEASE CITE THIS ARTICLE AS DOI: 10.1063/5.0106785

II. OUTLINE OF NUMERICAL SIMULATIONS

A. Simulation model and initial equilibrium

We carry out numerical simulations of XMHD equations[23] on a two-dimensional (2D) plane, keeping three components of a vector field. The XMHD equations read as

$$\frac{\partial \rho}{\partial t} = -\frac{\partial \left(\rho u_j\right)}{\partial x_j}, \tag{1}$$

$$\frac{\partial \left(\rho u_i\right)}{\partial t} = -\frac{\partial}{\partial x_j}\left(\rho u_i u_j + p\delta_{ij}\right) + \epsilon_{ijk} J_j B_k + \frac{\partial \Pi_{ij}}{\partial x_j} - \rho g \delta_{j,2}, \tag{2}$$

$$\frac{\partial p}{\partial t} = -u_k \frac{\partial p}{\partial x_k} - \Gamma p \frac{\partial u_j}{\partial x_j} + (\Gamma - 1)\left(\eta J_k J_k + u_i \frac{\partial \Pi_{ij}}{\partial x_j}\right), \tag{3}$$

$$\frac{\partial B_i}{\partial t} = -\epsilon_{ijk} \frac{\partial E_k}{\partial x_j}, \tag{4}$$

$$\frac{\partial B_k}{\partial x_k} = 0, \tag{5}$$

$$E_i = -\epsilon_{ijk}\left(u_j - \frac{\epsilon_H}{\rho} J_j\right) B_k - \frac{\epsilon_H}{\rho}\frac{\partial p_e}{\partial x_i} + \eta J_i. \tag{6}$$

The thermodynamic variables ρ, p are the mass density and the pressure, respectively. Plasma is assumed to be an ideal gas: $p = \rho T$, where T is the temperature. The variables with a single subscript u_i, B_i, E_i, and $J_i = \epsilon_{ijk}\partial_j B_k$, are the i-th vector component of the velocity, magnetic, electric, and current density fields, respectively. The subscripts are for $i = 1{,}2{,}3$ (or x, y, z, equivalently). For our 2D 3-component computations in this paper, we set $\partial_3 \equiv \partial_z = 0$. We take a sum from 1 to 3 for a repeated suffix. The gravity term $-\rho g \delta_{j,2}$ works in the $-y$ direction. (The gravity is set $g = 1$ all through this paper.)

The variables with multiple subscripts Π_{ij} and ϵ_{ijk} are the gyro-viscous tensor and the Levi-Civita's anti-symmetric tensor, respectively. The gyro-viscous tensor is given as

$$\Pi_{11} = \Pi_{22} \;=\; -\epsilon_G \frac{p_i}{2}\left(\frac{\partial u_2}{\partial x_1} + \frac{\partial u_1}{\partial x_2}\right), \tag{7}$$

$$\Pi_{12} = \Pi_{21} \;=\; -\epsilon_G \frac{p_i}{2}\left(\frac{\partial u_1}{\partial x_1} - \frac{\partial u_2}{\partial x_2}\right), \tag{8}$$

and $\Pi_{ij} = 0$ otherwise, assuming $p_i = p_e = p/2$. The parameters ϵ_H and ϵ_G represent the two-fluid (Hall) and the finite ion Larmor radius effects, respectively.

The equations (1)-(8) are already normalized by some representative quantities: the mass density ρ_0, a typical length L_0, the mean toroidal magnetic field B_T, the vacuum permeability μ_0, the Alfvén velocity $V_A = \sqrt{B_T^2/\mu_0\rho_0}$, and the Alfvén time unit $\tau_A = L_0/V_A$. The symbol

Γ denotes the ratio of the specific heats, $\Gamma = 5/3$. Basic variables ρ, p, u_i, and B_i are evolved in the time-direction keeping the equilibrium components within themselves.

Our numerical simulations are carried out by the use of the MUTSU/MINOS code which has been developed originally for simulations of instability of the Large Helical Device[24–27]. A difference of numerical techniques in this paper from those used in the original MINOS simulations in the literature is that the fourth-order central finite difference scheme is used instead of the eighth-order compact finite difference scheme. Numerical precision and intrinsic resolution associated with the choice of the numerical techniques have been verified in Refs. [20, 21] through a comparison with linear stability analysis.

In addition to the XMHD equations (1)-(8), we add a fourth-order hyper-diffusivity at the right-hand-side of eqs.(2) and (4), since an XMHD simulation requires a very high numerical resolution, as we can see in Ref.[20, 21]. In Ref.[21], the tail of energy spectra of the velocity and magnetic fields of Rayleigh-Taylor turbulence extends to a scale as small as the electron scale, unless being terminated by either normal or hyper-diffusivity.

B. The basic concept of a CITM and initial equilibrium for CITM simulations

A schematic image of the CITM is presented in Fig.1. In our simulation, the $x = x_1$ coordinate is for an azimuthal direction (with the periodicity 2π) and $-y = -x_2$ is for the radial direction, bounded by $y_S \le y \le y_N$. Here we set $y_N = 1$, $y_S = -1$, and $y_0 = 0.125$. Magnetic shear exists in the region $-y_0 \le y \le y_0$, and the pressure gradient balances the Lorentz force. Resistivity increases in the radial direction, in order to keep the current level low outside the LCFS. A fixed solid-wall boundary condition (BC) is imposed both at $y = y_N$ and $y = y_S$. This BC differs from that in our earlier work[14], in which a slip boundary condition is imposed both at $y = y_N$ and $y = y_S$.

A force-balanced equilibrium state is given as

$$\rho = \begin{cases} \rho_S, & (y \le -y_0) \\ \left(\frac{\rho_N - \rho_S}{2y_0}\right)(y + y_0) + \rho_S, & (-y_0 \le y \le y_0) \\ \rho_N, & (y \ge y_0) \end{cases} \tag{9}$$

$$p = \begin{cases} p_S, & (y \le -y_0) \\ \left(\frac{p_N - p_S}{2y_0}\right)(y + y_0) + p_S, & (-y_0 \le y \le y_0) \\ p_N, & (y \ge y_0) \end{cases} \tag{10}$$

$$B_x = \begin{cases} -B_0, & (y \le -y_0) \\ \left(\frac{B_0}{y_0}\right)(y + y_0) - B_0, & (-y_0 \le y \le y_0) \\ B_0, & (y \ge y_0), \end{cases} \tag{11}$$

$$B_y = 0, \tag{12}$$

$$u_x = 0, \tag{13}$$

$$u_y = 0, \tag{14}$$

$$u_z = 0 \tag{15}$$

as an initial condition for our CITM simulations. A part of the equilibrium component $b_z = B_{Z0}$ is determined to satisfy the equilibrium equations

$$0 = -\frac{\partial p}{\partial x_i} + \epsilon_{ijk} J_j B_k, \tag{16}$$

and $B_{Z0} = B_T$ at $y = 0$. The parameters ρ_S, ρ_N, T_N, T_S, and B_0 are given a control parameter. Since the mass density, pressure and temperature are related with each other by the equation of state of an ideal gas, we can give two of the three variables at the boundaries N and S. We give ρ_N, ρ_S, T_N, and T_S at the boundaries. Then p_N and p_S are determined automatically. Another parameter, $\beta = 2p/(B_x^2 + B_y^2 + B_z^2)$ at $y = 0$ is also given in the initial step of a numerical simulation to determine the mean pressure level. Then p_N and p_S are determined by the equation of the state of an ideal gas. The initial velocity field u_i, given in eqs.(9)-(16), is perturbed by sinusoidal functions with small amplitudes and random phases at each wave number in the x-direction.

As has been mentioned already, plasma should be nearly current-free at the SOL region, due to the divertor sheaths created by a fast electron transport toward the divertor. In order to enforce this status in a numerical simulation, we adopt the SOL diffusivity model

$$\eta = \left[2 - tanh\left(\alpha_1\left(\rho - \rho_{crit}\right)\right)\right]^{\alpha_2} \times \eta_0. \tag{17}$$

AIP Publishing Physics of Plasmas ACCEPTED MANUSCRIPT

This is the author's peer reviewed, accepted manuscript. However, the online version of record will be different from this version once it has been copyedited and typeset.

PLEASE CITE THIS ARTICLE AS DOI: 10.1063/5.0106785

which has been proposed in Ref.[14]. Equation (17) gives a large diffusivity at the region of $\rho \ll \rho_{crit}$ ($y < -y_0$) while $\eta \sim \eta_0$ is small at the region of $\rho \gg \rho_{crit}$ ($y > y_0$). (See Fig.1(b) for the profile of this diffusion model.) The parameters α_1 and α_2 denote the width of the transition layer between the two regions, and the amplification of the resistivity in the SOL layer against the pedestal region, respectively. There are some control parameters, α_1, α_2, ρ_{crit}. Based on the study in Ref.[14], we set $\alpha_1 = 8\pi$ and $\alpha_2 = 12$. Although ρ_{crit} can remain as a free parameter, we have verified that this parameter does not cause an essential change of numerical results presented in this paper. Thus we set $\rho_{crit} = (\rho_N + \rho_S)/2$ throughout this paper.

We note that the magnetic field should be open outside the LCFS of a divertor tokamak with separatrix, while the shear-slab configuration itself does not provide such open-field magnetic field lines. However, by introducing the SOL diffusivity model (17), one aspect of an open-field configuration, namely a low-level saturation of the current, can be expressed by a large resistivity outside the LCFS. In other words, we simulate by the use of the SOL diffusivity model a situation such that a transition from the interchange to the tearing mode can occur in an open magnetic field region where the effective η is quite large. We may be able to apply this model to a divertor tokamak with the separatrix by adjusting parameters in (17) more likely for the device. We do not proceed to this adjustment in this article in order to concentrate on investigating the robustness of the CITM to extended MHD effects in the shear-slab geometry.

III. NUMERICAL RESULTS

A. Outline of numerical simulations

Numerical simulations are carried out for the parameter sets shown in Table I. The plasma beta is fixed $\beta = 5\%$ throughout this paper. While run 0 is a traditional resistive MHD simulation with a constant and uniform resistivity, runs 1-8 are simulations with the SOL diffusion model. Non-ideal MHD parameters in runs 2-8 are $\epsilon_H = 0.05$ and $\epsilon_G = 0.01$. A finite-amplitude initial flow is given in runs 3-8. Although we have carried out other sets of parameters, we restrict ourselves to these in order to simplify our discussion to the growth of a CITM.

AIP Publishing Physics of Plasmas ACCEPTED MANUSCRIPT
This is the author's peer reviewed, accepted manuscript. However, the online version of record will be different from this version once it has been copyedited and typeset.
PLEASE CITE THIS ARTICLE AS DOI: 10.1063/5.0106785

We recall that the initial condition in eqs.(9)-(15) is not an equilibrium solution for a finite (non-zero) u_N. An azimuthal flow u_x with a finite u_N induces a non-equilibrium electric field in the y-direction (E_r in a toroidal plasma) through the multiplication of $u_x \times B_{Z0}$. We keep in mind that, since this velocity perturbs the initial equilibrium strongly, we cannot set u_N very large from the point of view of plasma linear stability analysis.

We fix a number of grid points in our simulations $N_x = 512$ in the x-direction and $N_y = 1024$ in the y-direction for the geometry of $2\pi \times (y_N - y_S)$ ($y_0 = 0.125$ here). We have carried out numerical simulations with both a smaller and larger number of grid points for some of the parameter sets in Table I, and have verified that the change of the maximum resolution does not influence the physical views studied in this paper. Thus we concentrate on computations with $N_x = 512$ and $N_y = 1024$.

B. Appearance of current-interchange tearing modes - verification of earlier results

Firstly, we verify that changes of the boundary conditions from the previous work[14] does not affect qualitative views of the growth of a CITM obtained by a resistive MHD simulation. In Fig.2(a), a color map of the mass density and magnetic field lines drawn by the use of the (x, y) vector components of run 0 are shown. Mushroom-like structures associated with the interchange instability grow in the mass density field, as we can expect from earlier works such as Ref.[14]. Although small ellipses, which suggest occurrence of magnetic reconnection due to a hyper-diffusivity, are observed, such an artificial magnetic reconnection does not spoil the growth of the interchange modes.

In Fig.2(b), a color map of the mass density and the 2D magnetic field lines of run 1, which has been carried out together with the SOL diffusivity model (17), are shown at the same moment as in Fig.2(a). A transition from an interchange mode to a tearing mode, induced by a plasma displacement toward a region of a large η, is observed as a generation of magnetic islands. This transition is the key-process of a CITM.

We note here for a susceptibility of the shear slab configuration to multiple modes. In a massive simulation, every types of modes of interchange, ripple and tearing modes may develop[28]. We can only discuss the key factor or our focus there. Since we find that the field line reconnection is the main factor, we therefore may exclude the interchange or

AIP Publishing Physics of Plasmas ACCEPTED MANUSCRIPT
This is the author's peer reviewed, accepted manuscript. However, the online version of record will be different from this version once it has been copyedited and typeset.
PLEASE CITE THIS ARTICLE AS DOI: 10.1063/5.0106785

rippling modes as the key factors and focus on the tearing modes. We further find that the tearing modes at edge is closely related to the current gradient (or resistivity gradient). This is simply because the plasma edge is special: one side is the plasma torus with closed field lines, the other side is SOL with field lines open to the divertors as we have modeled by the use of the SOL diffusivity model (17). This difference leads to a current jump across the last closed flux surface. While the resistivity gradient effects have been considered by Furth et al.[28] mainly for rippling modes, the convective contribution ($-\xi \cdot \nabla\sigma$) of current sheet (ξ is the displacement vector and $\sigma = 1/\eta$) that drives CITM has not been considered in the Furth's work for tearing modes. We therefore relates the phenomena to CITMs. The difference between the CITM and the conventional tearing modes [28] has been discussed in Ref.[12].

As the consequence of the transition, the growth of the interchange modes is suppressed, and so are the deformation of the mass density and magnetic fields. The most dominant Fourier wave-number in the nonlinear stage of the time-evolution can be found in run 1 at $k_x = 12$, while the most dominant Fourier wave-number of run 0 is $k_x = 9$. As above, we confirm that the growth of a CITM is observed as in Ref.[14] and that the change of the boundary condition at $y = y_N$ and $y = y_S$ does not affect the growth of a CITM.

C. Non-ideal effects on current-interchange tearing modes

While runs 0 and 1 are resistive MHD simulations, runs 2-8 are XMHD simulations with the non-ideal MHD effects. Figure 3(a) shows a color map of the mass density and the 2D magnetic field lines in run 2, at the same moment of the simulation as that in Fig.2. The magnetic islands generated by the growth of the tearing modes (the second phase of a CITM) are somewhat deformed in the x (azimuthal) direction. We also find that stripe patterns of low and high mass density are formed in the figure. (For a printed version of this paper, a quarter of this figure is shown in Fig.3(b) in black-and-white.) We come to this stripe pattern formation later.

The growth of the unstable modes is studied more closely by defining the energy spectra of the magnetic and velocity fields by the use of the Fourier transform of a variable into the

AIP Publishing Physics of Plasmas ACCEPTED MANUSCRIPT
This is the author's peer reviewed, accepted manuscript. However, the online version of record will be different from this version once it has been copyedited and typeset.
PLEASE CITE THIS ARTICLE AS DOI: 10.1063/5.0106785

x-direction as:

$$E_{M_{2D}}\left(k_x,t\right)=\frac{1}{(y_N-y_S)}\int dy\left(\left|\widetilde{B}_x\left(k_x,y,t\right)\right|^2+\left|\widetilde{B}_y(k_x,y,t)\right|^2\right)/2, \tag{18}$$

$$E_K\left(k_x,t\right)=\frac{1}{(y_N-y_S)}\int dx\left(\left|\widetilde{u}_x\left(k_x,y,t\right)\right|^2+\left|\widetilde{u}_y(k_x,y,t)\right|^2+\left|\widetilde{u}_z(k_x,y,t)\right|^2\right)/2, \tag{19}$$

where $\widetilde{\cdot}(k_x,y)$ is the Fourier-transform of a variable in the x-direction. The z-component of the magnetic field field B_z is omitted from the definition of $E_{M_{2D}}$ because the z-component in the equilibrium is too large to see fluctuations of the other components, while all three components are kept in the definition of E_K.

Figure 4 is a time-evolution of $E_{M_{2D}}$ for $k_x \leq 20$ in (a) run 1 and (b) run 2. We can find a difference between them in the growth of the energy at each k_x: a single-step jump (or a nonlinear acceleration) at $t \simeq 2.5$ in (a) run 1 and two-step jumps at $t \simeq 1.8$ and 3 in (b) run 2. Furthermore, the $k_x = 20$ mode becomes the most dominant in (b) by an acceleration at $t \simeq 2.5$ (only by a single-step jump for this mode), while it remains comparable to the $k_x = 18$ mode in (a). Since these accelerations and the reconnection of the magnetic field lines are observed at about the same time, we consider that the acceleration is triggered by the magnetic reconnection.

We note that the dominance by $k_x = 20$ is considered as a consequence as the two-step transition of instability from interchange to tearing modes. One possible understanding is that this dominance can be closely related with the extended MHD effects associated with the Hall term because the parameter $\epsilon_H = 0.05$ indicates that the extended MHD effect by the Hall term is dominant at the scale. With respect to a higher scale which is not presented in the figure, the other extended MHD effects associated with the gyro-viscous term is considered to suppress the growth of the interchange or a pressure-driven mode. (Please also see Refs.[19–21] and references therein.)

We also note that the growth rate in runs 0 and 1 are estimated by additional computations of the linearized version of eqs.(1)-(6). We have also checked the profile of the Fourier coefficients for separate k_x as the function of y for the two runs. See Appendix for these additional results.

Figure 5 represents a time-evolution of E_K for $k_x \leq 20$ in (a) run 1 and (b) run 2. The energy of the $k_x = 0$ mode jumps to a finite level both in (a) and (b) at the beginning of the simulations. This jump is generated by a small but finite non-equilibrium component of the initial condition in eqs.(1)-(6) such as the $\partial p_e/\partial x_i$ term in eq.(6). In contrast to Fig.4,

AIP Publishing Physics of Plasmas ACCEPTED MANUSCRIPT
This is the author's peer reviewed, accepted manuscript. However, the online version of record will be different from this version once it has been copyedited and typeset.
PLEASE CITE THIS ARTICLE AS DOI: 10.1063/5.0106785

Fig.5 exhibits a clear difference between runs 1 and 2 in the $k_x = 0$ mode. While the $k_x = 0$ mode does not grow large in (a), it begins nonlinear growth as the time of the magnetic reconnection comes, and evolves to the most-dominant Fourier-mode in the final time of the simulation in (b). This represents a gradual formation of a finite-amplitude dia-magnetic drift flow. The growth of the $k_x = 0$ mode is contributed to by the gyro-viscosity, which provides a nonlinear coupling of the pressure fluctuation and the velocity gradient tensor in eqs.(7) and (8).

The observations above show that the growth of a CITM is not suppressed by the non-ideal MHD effects, simply because they do not suppress growth of an interchange mode completely, as we can see in Ref.[19, 21, 22]. In other words, growth of a CITM can trigger an ELM-free current eruption through a transition from an interchange mode to a tearing mode at a plasma edge region.

D. Response to an externally-imposed flow

In a toroidal plasma, edge plasma is exposed to various kind of flows or flow shears excited in the plasma core side by an intrinsic mechanism (such as the $E \times B$ drift) and/or by an extrinsic process such as a beam injection. The response of a CITM to such a flow can be examined quickly by setting a finite azimuthal flow u_x, with an initial (non-equilibrium) flow

$$u_x = \begin{cases} u_S, & (y \leq -y_0) \\ \left(\frac{u_N - u_S}{2y_0}\right)(y + y_0) + u_S, & (-y_0 \leq y \leq y_0) \\ u_N. & (y \geq y_0) \end{cases} \tag{20}$$

The flow is driven as the boundary condition $u_x = u_N$ ($u_x = u_S$) at the $y = y_N$ ($y = y_S$) boundary wall. Although this flow includes a flow shear, the shear is linear to the y-coordinate and thus does not generate momentum through the gyro-viscosity. This enables us to forget a momentum transfer between the x and y components of the momentum field equation (2) by the gyro-viscosity, and focusing on an effect of the flow through the Reynolds stress term in eq.(2) and the dynamo term in eq.(6).

The flow parameter u_N is given in Table 1. We keep $u_S = 0$ throughout this article. By the use of a typical middle-size torus device parameters (minor radius $\sim 0.5m$, toroidal magnetic field $B_T \sim 3T$, the number density $n \sim 10^{19}/m^3$, for example), a dimensional velocity for $u_N = 1 \times 10^{-6}$ can be estimated as in the order of $0.1m/s$, which is in the same

AIP Publishing Physics of Plasmas ACCEPTED MANUSCRIPT
This is the author's peer reviewed, accepted manuscript. However, the online version of record will be different from this version once it has been copyedited and typeset.
PLEASE CITE THIS ARTICLE AS DOI: 10.1063/5.0106785

order as the diamagnetic drift velocity of an edge plasma, while $u_N = 10^{-2}$ is in the order of $10^3 m/s$ which is roughly comparable to the core rotation velocity.

Figure 6 is a color map of the mass density and 2D magnetic field lines in (a) run 3 ($u_N = 1 \times 10^{-6}$) and (b) 4 ($u_N = -1 \times 10^{-6}$) at the same moment as those in Figs.2 and 3. Both Fig.6(a) and (b) are very similar to Fig.3(a), in which the magnetic islands associated with a tearing mode (the second stage of a CITM) are deformed, as in runs 1 and 2.

In Fig.7, a time-evolution of the Fourier energy in (a) run 3 and (b) run 4 is shown. The time evolution of $E_{M_{2D}}$ at each k_x shows frequent jumps and drops in time. These jumps and drops suggest a strong coupling of the CITM with an externally-driven flow, resulting in rapid growth and minor collapse. Nevertheless, the color map and magnetic field lines in Fig.6 retain characteristics of the CITM (O-points of the magnetic field lines and a small radial displacement), indicating that the growth of the CITM is robust against influences of a small but finite externally-driven azimuthal flow. We note that the difference in (a) and (b) is quite small. This means that, whichever the external flow and the consequent E_r direction might be, the radial displacement associated with $|u_N| = 1 \times 10^{-6}$ can induce the transition to the tearing mode. In the case of outward E_r, this E_r can trigger transition to the tearing mode directory. In the case of inward E_r, a region of low ρ (and thus a high η due to the SOL diffusivity model) comes to a strong magnetic shear region and induces the transition to the tearing mode.

In the series of XMHD simulations (runs 3-8), we have increased the driving velocity $|u_N|$. Figure 8 is a color map of the mass density and 2D magnetic field lines in (a) run 5 ($u_N = 1 \times 10^{-4}$) and (b) 7 ($u_N = 1 \times 10^{-2}$) at the same moment as those in Figs.2, 3 and 6. The magnetic field lines in Fig.8(a) and (b) are similar to those in Fig.2(a) in which interchange modes grow, and very different from those in Fig.2(b), Figs.3 and 6. In Fig.9, the growth of the magnetic Fourier energy of (a) run 5 and (b) run 7 is presented. There is no small jump nor drop in the time evolution, showing a simple interchange-like growth, even though both the non-ideal MHD effects and the SOL diffusivity model are included in the simulations. As in Figs.8 and 9, both the magnetic field lines and the Fourier energy growth are quite different from those in runs 1-4. Those observations indicate disappearance of the CITM due to a large $|u_N|$.

The disappearance is attributed to induction of the electric field in the radial direction. A finite initial u_x induces the y-component of the electric field (E_r in a torus plasma) through

$u_x \times B_Z$ in the generalized Ohm's law (6). As is well-known, E_r causes a plasma displacement in the radial direction. On an occasion of a large $|u_N|$, a large radial displacement due to the E_r effect inhibits a transition from an interchange to a tearing mode. In this sense the growth of the CITM under a finite flow is subject to the amplitude of the flow which causes E_r-originated displacement.

It may be noteworthy here that the autonomously-generated azimuthal flow ($k_x = 0$ mode) is strongest in runs 3 and 4 among all runs, although we do not see plots of E_K very closely for each of runs 1-8. In runs 3 and 4, the $E_K(k_x = 0, t)$ grows a few times larger than that given by the externally-driven flow. On the other hand, the $E_K(k_x = 0, t)$ in runs 5 and 6 does not grow very large, even though the externally-driven flow is 100 times stronger than that in runs 3 and 4. Consequently the $E_K(k_x = 0, t)$ in runs 3 and 4 is much larger than that in runs 5 and 6. In runs 7 and 8, the $E_K(k_x = 0, t)$ stays almost constant. This means that the externally-driven flow dominates a flow field and autonomous flow generation is quite minor. These may provide us a new subject to study nonlinear flow interactions at an edge region.

E. Formation of a stripe pattern in the mass density field

In Fig.3, we observed a formation of a stripe pattern. This pattern somewhat look similar to so-called streamers in the sense that $k_r = 0$ and $|k_\theta| > 1$ where k_r and k_θ are the radial and poloidal wavenumber in terms of a toroidal configuration, respectively. Streamers have been studied extensively, sometimes together with zonal flows, in the context of turbulent transport. (See Refs.[29–35] and references therein.) In order to concentrate on the non-ideal MHD effects on a CITM in its growing stage, we do not pursue detail of this streamer-like stripe structure. Instead we verify how this structure is formed at the growing stage by comparing the structures in runs 1 and 2.

Figure 10 represents the mass density fluctuation plotted on the lines of (a) $y = 0.25$, (b) $y = 0$ (on the LCFS), and (c) $y = -0.25$ at time $t = 5$, 5.5, 6, 6.5, 7 and 7.5. In order to see plots closely, we restrict the range of the horizontal axis to $-0.5 \leq x \leq 0.5$. In Figs.10(a) and (b), the mass density fluctuation grows on the LCFS without a disturbance in the phase of the fluctuation of the mass density field. It is easily seen that the growth is almost saturated at $t \simeq 7$, and that the most dominant wave-number, k_x, of the structure in

AIP Publishing Physics of Plasmas ACCEPTED MANUSCRIPT
This is the author's peer reviewed, accepted manuscript. However, the online version of record will be different from this version once it has been copyedited and typeset.
PLEASE CITE THIS ARTICLE AS DOI: 10.1063/5.0106785

(a) is larger than that in (b). (The most dominant k_x of the stripe structure in the vicinity of the LCFS is comparable to that of the most dominant Fourier mode of the CITM.) The mass density fluctuation in (c) is more irregular than those in the other two panels, (a) and (b). Considering the symmetry of the governing equations (1)-(6) and the initial condition in eqs.(9)-(15) with respect to the LCFS, the asymmetry between (a) and (c) is attributed to the suppression of the current density by the SOL diffusivity model at $y < 0$.

Figure 11 represents the mass density fluctuation plotted on the lines of (a) $y = 0.25$, (b) $y = 0$ (on the LCFS), and (c) $y = -0.25$ of run 2 at the same moments as in Fig.10. A clear difference between Figs.10 and 11 can be found in the panel (b) of the two figures. While the mass density fluctuation in Fig.10(b) does not drift but grows at the same place, the mass density travels toward the positive-x direction on the LCFS, as can be seen in Fig.11(b). This is a clear consequence of the non-ideal MHD effects, by which a dia-magnetic drift motion has been induced. The drift velocity V_D is estimated from Fig.11(b) as $V_D \simeq 0.15$. This value is comparable to the $E_K(k_x = 0, t)$ in Fig.5 at the final moment. We also find that the mass density fluctuation grows and saturates without drift velocity motion in Fig.11. This is natural because the pressure gradient is small at $y \simeq \pm 0.25$, where (a) and (c) are plotted, and thus a drift motion is not induced.

In Fig.12, the mass density ρ, the dilatation $\partial u_i/\partial x_i$, the third component of the vorticity $\epsilon_{3jk}\partial u_k/\partial x_j$, and (x, y) components of the electric field of run 2 at $t = 7$ are shown on the same lines as Fig.11. The dilatation $\partial u_i/\partial x_i$ and the vorticity are scaled by the same factor. In Fig.12(a), all the quantities show a very high coherence with each other. More specifically, plots of the x-component of the electric field and the fluid dilatation $\partial u_i/\partial x_i$ represent that the stripe pattern of the mass density fluctuation is generated through the dilatation term in eq.(1) by the x-component of the electric field. We also find that the dilatation and the vorticity are comparable to each other, representing that a fluid compressibility plays a crucial role there. The y-component of the electric field is small at $t = 7$.

In Fig.12(b), in contrast to (a), the vorticity is much larger than the dilatation, and show an apparent correlation with the mass density fluctuation, especially in the regions $x < -0.2$ and $x > 0.2$. Even in the region $-0.2 \leq x \leq 0.2$, although some of the local maxima/minima of the density may look correlating rather with the dilatation than with the vorticity, relatively large maxima/minima of the mass density correlates with the vorticity. This tendency is persistent after the CITM growth in finite an amplitude. This suggests

AIP Publishing Physics of Plasmas ACCEPTED MANUSCRIPT
This is the author's peer reviewed, accepted manuscript. However, the online version of record will be different from this version once it has been copyedited and typeset.
PLEASE CITE THIS ARTICLE AS DOI: 10.1063/5.0106785

that strong vortices generated by a CITM dominate physics in this region, and other effects can be dropped from discussion. The plots in Fig.12(c) are rather similar to those in (a) rather than (b). Oscillatory patterns of E_x show an apparent synchronization with those of the mass density and dilatation.

Similar behaviors of the mass density fluctuation, dilatation, vorticity and electric field as above, can be seen commonly among runs 1-8. In runs 5-8, in which interchange modes grow to a large amplitude, the formation of these structures is relatively unclear and irregular (in the region of the higher side of the mass density especially), because a large deformation of the mass density and other quantities is caused in association with violent interchange modes, not by a static compression/dilatation associated with the growth of a CITM. On the other hand, with respect to numerical simulations in which the non-ideal MHD effects apparently emerge (such as runs 2, 3, and 4), the stripe structures are elongated in the radial direction, being parallel to each other.

The formation of the stripe patterns reminds us of so-called streamers. According to earlier studies on streamers (and zonal flows as well) [29–35], a streamer is understood as a large convective cell. In this context we can expect that a fluctuation is advected in the direction of a large-scale convection if the stripe-structures are streamers. To the contrary, the wavy or stripe-structures observed in our study appear as the consequence of a fluid compression/dilatation, and stay without traveling throughout the growing stage of a CITM, showing a standing-wave-like nature. Although the stripe pattern can be advected in a long period (in transport-time-scale) once the growing stage is over, we recognize that the stripe-structures can be somewhat different from streamers.

In the end of this subsection, formation of the stripe structure is summarized as follows. The typical wave-length is comparable to that of the most unstable mode of the CITM, being closely related with the occurrence of CITM, or a transition to the tearing mode. The drift velocity computed from the stripe structure $V_D = 0.15$. This drift velocity is in the order of $10^3 - 10^4 m/s$, being comparable to a typical poloidal rotation speed in the plasma core side) in a typical middle-size torus experiment. (See Ref.[36], for example.) Since the drift velocity coincides with the plasma core rotation velocity, the formation of a structure may play some finite role in a real physics, too. However, the discussion above remains as a conjecture yet and we need further study about this issue. Thus we restrict ourselves to report simply that a structure formation which may look like a streamer but have some different characteristics from streamers is observed in our simulations.

IV. CONCLUDING REMARKS

We have studied non-ideal MHD effects on the growth of a CITM by means of extended MHD simulations, combined with the SOL diffusivity model. We have shown that a CITM can grow under the non-ideal MHD effects, as well as under the presence of a weak azimuthal flow. However, for a strong azimuthal flow, a CITM can be suppressed because E_r generated by the flow suppresses the transition from an interchange mode to a tearing mode. Consequently, an interchange mode can grow large under the presence of a large flow. Since an azimuthal flow can be generated by various processes in experiments, we need further studies, including a more realistic flow.

In our simulations, a stripe pattern similar to a streamer is observed both in the high and low mass density regions. A fluid compression and dilatation associated with the electric field induced in the course of the CITM growth plays a crucial role in the structure formation. The fluid dilatation can be as large as the vorticity in the higher or lower density region, suggesting that a 2D model which keeps only the vorticity in a set of the equations does not reproduce the structure.

With respect to study non-ideal MHD effects, the meaning of the results above are two-fold. From a point of view of studying the robustness of CITM to the extended MHD effects, the CITM is robust and consequently the extended MHD effects are not very essential. This result supports the meaning of studying CITM as a primitive model of an edge plasma instability. From a point of view of studying the CITM as a primitive model of ELM-related events, the introduction of the extended MHD effects brings about generations of diamagnetic flow, formation of a flow shear, and interaction with small islands. While we place a higher priority on the first point in this paper, these physical effects can be more important in a toroidal configuration. Thus the numerical results presented in this numerical study provide information for this purpose.

This research is partially supported by JSPS KAKENHI Grant Number 17K05734 and 20H00225, Japan, and Department of Energy Grants DE-FG02-04ER54742. This research is also partially supported by the Joint Institute for Fusion Theory (JIFT) program in the US-Japan collaboration for fusion studies. The numerical simulations were performed on *Plasma Simulator* of NIFS (FUJITSU FX100 supercomputer until February 2020, the NEC SX-Aurora TSUBASA A412 since July 2020) with the support and under the auspices of the NIFS Collaboration Research program (NIFS19KNSSS114, NIFS19KNTS059, NIFS20KNSSS133, NIFS20KNTS063), as well as on *Oakforest-PACS* (FUJITSU) of the JC-AHPC, and *Wisteria/BDEC-01 Odyssey* (FUJITSU FX1000) of the University of Tokyo, being supported by the Joint Usage/Research Center for Interdisciplinary Large-Scale Information Infrastructures in Japan (jh190006-NAJ, jh200002-NAH,jh210004-NAH,jh220005).

APPENDIX

In this Appendix, we present additional results obtained by computations of the linearized version of eqs.(1)-(6). The linear computations are carried out without the SOL diffusivity corresponding to run 0, and with the SOL diffusivity corresponding to runs 1 and 2, respectively. Thus these linear computations are also referred to runs 0-2 in this Appendix. In runs 1 and 2, the SOL diffusivity is linearized for a small mass density fluctuation. These additional computations are carried out so that readers can see linear aspects of the CITM.

In Fig.13, the growth rate at the exponentially growing stage is presented as a function of k_x for run 0 (box), run 1(filled circle), and run 2 (triangle). The growth rate of run 0 increases as k_x becomes large, and then decreases gradually for $k_x \geq 12$. Since the interchange mode has a larger growth rate for a larger wave number, the peak of the growth rate at $k_x = 11$ means that the wave number region $k_x \geq 12$ is affected by the hyper-diffusivity. We remark that our earlier computations on the Rayleigh-Taylor instability gives a similar curve [20, 21]. In this sense, this linear computation is consistent with these earlier works.

While the growth rate of run 0 increases as the function of k_x for $k_x < 12$, the introduction of the SOL diffusivity model changes this property. The growth rate of run 1 in Fig.13 has a single peak at $k_x \simeq 5$, being comparable to (smaller than) that of run 0 presented at $k_x \leq 5$ ($k_x > 5$). An influence of extended MHD effects, the Hall effect, appears clearly in the growth rate of run 2. The linear growth rate of run 2 is larger than those of runs 0 and 1. We remember that the SOL diffusivity model brings about a strong suppression of the magnetic field outside the LCFS. This can bring about a sharp jump of the current density at $y \simeq 0$ (where $\rho \simeq \rho_{crit}$). It is considered that the sharp jump of the current density enhances an impact of the Hall term in run 2 while the jump does not influence run

AIP Publishing Physics of Plasmas ACCEPTED MANUSCRIPT

This is the author's peer reviewed, accepted manuscript. However, the online version of record will be different from this version once it has been copyedited and typeset.

PLEASE CITE THIS ARTICLE AS DOI: 10.1063/5.0106785

1 consequently.

Next, the cosine and sine parts of the Fourier component $\widetilde{B}_y$ (the radial component of the magnetic field) are presented in Fig.14 as functions of y for typical wave numbers of the parameter sets (a) run 0, (b) run 1, (c) run 2, and (d) run 5. The representative modes are chosen so that we can see the profiles of the lowest wave number $k_x = 1$ as well as the odd ($k_x = 7$) and the even ($k_x = 8$) wave number modes clearly. The normalization of the radial profile is arbitrary, being set so that the profiles of the different wave numbers can be distinguished from each other easily. See Figs.11 and 12 in the original CITM paper[12] for the CITM profiles which appear as transition from resistive interchange modes to CITMs in the cylinder limit.

In Fig.14(a), both the cosine and sine parts of the $k_x = 1$ and $k_x = 7$ modes, the odd modes, have their peak in $y < 0$ and bottom in $y > 0$, respectively. On the contrary, the cosine and sine parts of the even mode $k_x = 8$ have their peak and bottom in the same region: peak in $y > 0$ and bottom in $y < 0$. In this figure, the mode profile is smooth and symmetrical to $y = 0$, being associated with the symmetry of the system.

On the contrary, the mode profile in Fig.14(b) is asymmetric to $y = 0$. This asymmetry in Fig.14(b) is similar to that in Figs.12 of Ref.[12], and attributed to the presence of the SOL diffusivity model in eq.(17). Furthermore, the Fourier mode profile is more localized at $y \simeq 0$ than that in Fig.14(a), although the basic profile for even/odd wave-numbers are kept the same as that in Fig.14(a). This localization is considered to arise from a large SOL diffusivity introduced in run 1.

The Fourier mode profile of run 2 is shown in Fig.14(c). The Fourier coefficients have sharp peaks at $y \simeq 0$, being localized much more strongly than those in Fig.14(b). The strong localization is considered as the influence of the Hall term which takes a large value due to the jump of the current density associated with the SOL diffusivity near $y \simeq 0$.

At the end of this Appendix, we note that the growth rate in Fig.13(b) and (c) may require more careful estimation. Our linear computations with the linearization of the SOL diffusivity model suffer from a numerical instability more severely than corresponding nonlinear simulations, and need a larger hyper-diffusivity for stabilization than corresponding nonlinear simulations. This can contaminate the estimation of the growth rate. Since the linear mode analysis requires careful treatment, especially with respect to the estimation of the linear growth rate, we need further study on linear aspects of the CITM and the result in Fig.13(b),(c) and Fig.14(b),(c) may be corrected there.

[1] F. Wagner, G. Becker, K. Behringer, D. Campbell, A. Eberhagen, W. Engelhardt, G. Fussmann, O. Gehre, J. Gernhardt, G. v. Gierke, G. Haas, M. Huang, F. Karger, M. Keilhacker, Q. Kluber, M. Kornherr, K. Lackner, G. Lisitano, G. G. Lister, H. M. Mayer, D. Meisel, E. R. MIiller, H. Murmann, H. Niedermeyer, W. Poschenrieder, H. Rapp, H. Bohr, F. Schneider, G. Siller, E. Speth, A. Stabler, K. H. Steuer, G. Venus, O. Vollmer, and Z. Yü, Phys. Rev. Lett. **49**, 1408 (1982).

[2] K. Ikeda, Nucl. Fusion **47**, 1 (2007).

[3] E.J. Doyle, W.A.Houlberg, Y.Kamada, V.Mukhovatov, T.H.Osborne, A.Polevoi, G.Bateman, J.W.Connor, J.G.Cordey, T.Fujita, et al., Nucl. Fusion **47** S18 (2007).

[4] T.C. Hender, J.C.Wesley, J.Bialek, A.Bodeson, A.H.Boozer, R.J.Buttery, A.Garofalo, T.P.Goodman, R.S.Granetz, Y.Gribov, et al., Nucl. Fusion **47** S128 (2007) .

[5] A. W. Leonard, J. A. Boedo, M. E. Fenstermacher, R. J. Groebner, M. Goth, C. J. Lasnier, M. A. Mahdavi, T. H. Osborne, D. L. Rudakov, T. W. Petrie, J. G. Watkins, J. Nucl. Mater. **313-316**, 768 (2003).

[6] T. E. Evans, Plasma Phys. Control. Fusion **57** 123001 (2015) .

[7] R.A. Moyer, C. Paz-Soldan, R. Nazikian, D.M. Orlov, N.M. Ferraro, B.A. Grierson, M. Knölker, B.C. Lyons, G.R. McKee, T.H. Osborne et al., Phys. Plasmas **24** 102501 (2017).

[8] K.H. Burrell, W.P. West, E.J. Doyle, M.E. Austin, T.A. Casper, P. Gohil1, C.M. Greenfield, R.J. Groebner, A.W. Hyatt, R.J. Jayakumar et al., Phys. Plasmas **12** 056121 (2005).

[9] N. Aiba, X. Chen, T.H. Osborne, M. Honda, K.H. Burrell and P.B. Snyder, Nucl. Fusion 60 (2020) 092005.

[10] H. Takahashi, E.D. Fredrickson, M.J. Schaffer, M.E. Austin, T.E. Evans, L.L. Lao and J.G. Watkins, Nucl. Fusion **44**,1075 (2004).

[11] G. M. Staebler and F. L. Hinton, Nucl. Fusion **29**, 1820 (1989).

[12] L. Zheng, and M. Furukawa, Phys. Plasmas **17** 052508 (2010).

[13] L. Zheng and M. Furukawa, Phys. Plasmas **21**, 082515 (2014).

[14] H. Miura, L. Zheng, and W. Horton, Phys. Plasmas **24**, 092111 (2017).

[15] B. I. Cohen, M. V. Umansky, W. M. Nevins, M. A. Makowski, J. A. Boedo, D. L. Rudakov,

AIP Publishing Physics of Plasmas ACCEPTED MANUSCRIPT
This is the author's peer reviewed, accepted manuscript. However, the online version of record will be different from this version once it has been copyedited and typeset.
PLEASE CITE THIS ARTICLE AS DOI: 10.1063/5.0106785

G. R. McKee, Z. Yan, and R. J. Groebner, Phys. Plasmas **20**, 055906 (2013).

[16] B. J. Burke, S. E. Kruger, C. C. Hegna, P. Zhu, P. B. Snyder, C. R. Sovinec, and E. C. Howell, Phys. Plasmas **17**, 032103 (2010).

[17] X. Q. Xu, P. W. Xi, A. Dimits, I. Joseph, M. V. Umansky, T. Y. Xia, B. Gui1, S. S. Kim, G. Y. Park, T. Rhee, H. Jhang, P. H. Diamond, B. Dudson, and P. B. Snyder, Phys. Plasmas **20**, 056113 (2013).

[18] X. Liao, Z. Lin, I. Holod, Y. Xiao, B. Li, and P. B. Snyder, Phys. Plasmas **23**, 122507 (2016).

[19] P. Zhu, D. D. Schnack, F. Ebrahimi, E. G. Zweibel, M. Suzuki, C. C. Hegna, and C. R. Sovinec, Phys. Rev. Lett. **101**, 085005 (2008).

ha

[20] R. Goto, H. Miura, A. Ito, M. Sato, and T. Hatori, Plasma Fusion Res.**9** (2014) 1403076.

[21] R. Goto, H. Miura, A. Ito, M. Sato, and T. Hatori, Phys. Plasmas **22** (2015) 032115.

[22] A. Ito and H. Miura, Phys. Plasmas **23**, 122123 (2016).

[23] D.D.Schnack, D.C.Barnes, D.P.Brennan, C.C.Hegna, E.Held, C.C.Kim, S.E.Kruger, A.Y.Pankin, C.R.Sovinec, Phys. Plasmas **13** 058103 (2006).

[24] H. Miura, K.Ichiguchi, N.Nakajima, T.Hayashi, and B.A. Carreras, Proc. 20th IAEA-FEC TH2-3" (Nov.1-6, 2004, Villamoura, Portugal).

[25] H. Miura, N.Nakajima, T.Hayashi, and M.Okamoto, Fusion Sci. Tech. **51** pp.8-19 (2007).

[26] H. Miura and N. Nakajima, Nucl. Fusion **50** 054006 (2010).

[27] H. Miura, F. Hamba, and A. Ito, Nucl. Fusion **57** 076034 (2017).

[28] H.P. Furth, J.Killeen, and M.N.Rosenbluth, Phys. Fluids **6** 459-484 (1963).

[29] G Manfredi, C.M Roach, and R.O Dendy, Plasma Phys. Contr. Fusion, **43** pp.825-837 (2001).

[30] P.H. Diamond, S. Champeaux, M. Malkov, A. Das, I. Gruzinov, M.N. Rosenbluth, C. Holland, B. Wecht, A.I. Smolyakov, F.L. Hinton, Nucler Fusion **41** 1067-1080 (2001).

[31] J. Li, and Y. Kishimoto, Phys. Plasmas **15**, 112504 (2008).

[32] A.Ghizzo, D.Dei Sarto, X.Garbet, and Y.Sarazin, Phys. Plasmas **17**, 092501 (2010).

[33] N. Bisai and P. K. Kaw, Phys. Plasmas **25**, 012503 (2018).

[34] N.T. Howard, C. Holland, A.E. White, M. Greenwald, and J. Candy, Phys. Plasmas **21**, 112510 (2014).

[35] Y. Zhang and S. I. Krasheninnikov, Phys. Plasmas **27**, 122303 (2020).

[36] A.R Field, J.McCone, N.J Conway, M. Dunstan, S. Newton, and M. Wisse, Plasma Physics

and Controlled Fusion **51** 105002 (2009).

AIP Publishing Physics of Plasmas ACCEPTED MANUSCRIPT
This is the author's peer reviewed, accepted manuscript. However, the online version of record will be different from this version once it has been copyedited and typeset.
PLEASE CITE THIS ARTICLE AS DOI: 10.1063/5.0106785

Figure Captions

Figure 1 : (a) A schematic view of a CITM, and (b) SOL diffusivity model for the resistivity gradient across the LCFS.

Figure 2 : A color map of the mass density and 2D magnetic field line of (a) run 0 and (b) run 1.

Figure 3 : (a) A color map of the mass density and 2D magnetic field lines in run 2, and (b) magnification of (a) in black and white for the printed version.

Figure 4 : Fourier energy growth of the magnetic field in (a) run 1 and (b) run 2

Figure 5 : Fourier energy growth of the velocity field in (a) run 1 and (b) run 2.

Figure 6 : A color map of the mass density and 2D magnetic field lines in (a) run 3 and (b) run 4. The mass density is larger (or smaller) for a darker (or brighter) color.

Figure 7 : Fourier energy growth of the magnetic field in (a) run 3 and (b) run4.

Figure 8 : A color map of the mass density and 2D magnetic field lines in (a) run 3 and (b) run 4. The mass density is larger (or smaller) for a darker (or brighter) color.

Figure 9 : Fourier energy growth of the magnetic field in (a) run 5 and (b) run 7.

Figure 10 : Time variation of the mass density of run 1 at (a)$y = 0.25$, (b)$y = 0$, and (c)$y = -0.25$.

Figure 11 : Time variation of the mass density of run 2 at (a)$y = 0.25$, (b)$y = 0$, and (c)$y = -0.25$.

Figure 12 : The mass density, dilatation, vorticity, and electric field components of run 2 at (a)$y = 0.25$, (b)$y = 0$, and (c)$y = -0.25$.

Figure 13 : The linear growth rate in the linear computation corresponding to run 0 (box), run 1 (filled circle), and run 2 (triangle).

Figure 14 : The cosine and sine parts of the Fourier coefficients of $\widetilde{b}_2$ as the function of the y in the linear computations corresponding to (a) run 0, and (b) run 1, and (c) run 2.

AIP Publishing Physics of Plasmas ACCEPTED MANUSCRIPT
This is the author's peer reviewed, accepted manuscript. However, the online version of record will be different from this version once it has been copyedited and typeset.
PLEASE CITE THIS ARTICLE AS DOI: 10.1063/5.0106785

TABLE I. Parameters of numerical simulations

Run	β	ϵ_H	ϵ_G/B_Z	ρ_{crit}	$2y_0$	$\rho_N - \rho_S$	BC at $y = y_N$
0	0.05	0	0	–	0.25	0.75	fixed, $u_N = 0$
1	0.05	0	0	0.5	0.25	0.75	fixed, $u_N = 0$
2	0.05	0.05	0.01	0.5	0.25	0.75	fixed, $u_N = 0$
3	0.05	0.05	0.01	0.5	0.25	0.75	fixed, $u_N = 1 \times 10^{-6}$
4	0.05	0.05	0.01	0.5	0.25	0.75	fixed, $u_N = -1 \times 10^{-6}$
5	0.05	0.05	0.01	0.5	0.25	0.75	fixed, $u_N = 1 \times 10^{-4}$
6	0.05	0.05	0.01	0.5	0.25	0.75	fixed, $u_N = -1 \times 10^{-4}$
7	0.05	0.05	0.01	0.5	0.25	0.75	fixed, $u_N = 1 \times 10^{-2}$
8	0.05	0.05	0.01	0.5	0.25	0.75	fixed, $u_N = -1 \times 10^{-2}$

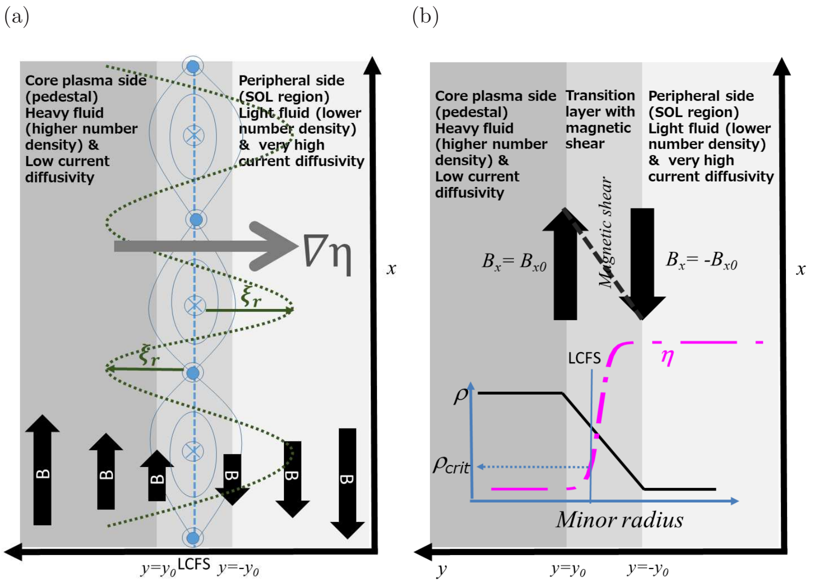
(a)
Core plasma side (pedestal) Heavy fluid (higher number density) & Low current diffusivity
Peripheral side (SOL region) Light fluid (lower number density) & very high current diffusivity
$\nabla\eta$
ξ_r
ξ_r
B
B
B
B
B
B
x
$y=y_0$
LCFS
$y=-y_0$
(b)
Core plasma side (pedestal) Heavy fluid (higher number density) & Low current diffusivity
Transition layer with magnetic shear
Peripheral side (SOL region) Light fluid (lower number density) & very high current diffusivity
Magnetic shear
$B_x = B_{x0}$
$B_x = -B_{x0}$
x
LCFS
η
ρ
ρ_{crit}
Minor radius
y
$y=y_0$
$y=-y_0$

FIG. 1. (a) A schematic view of a CITM, and (b) SOL diffusivity model for the resistivity gradient across the LCFS.

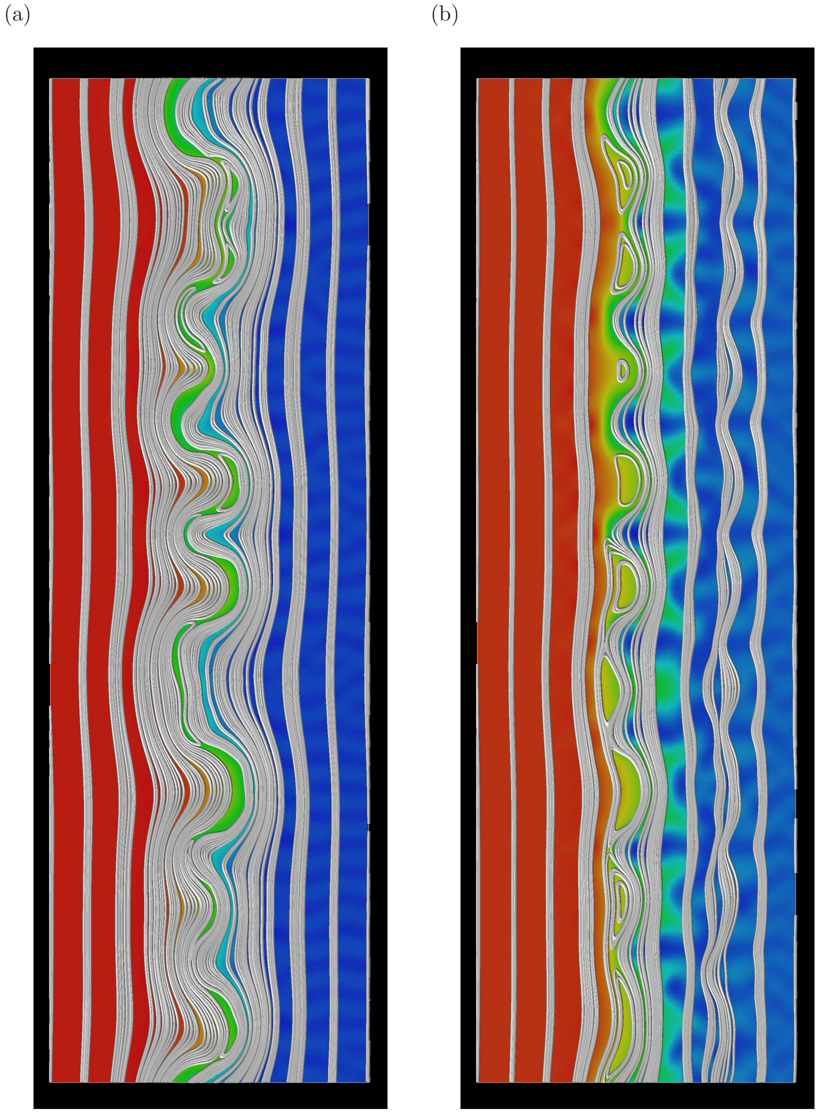

FIG. 2. A color map of the mass density and 2D magnetic field line of (a) run 0 and (b) run 1.

AIP Publishing Physics of Plasmas ACCEPTED MANUSCRIPT

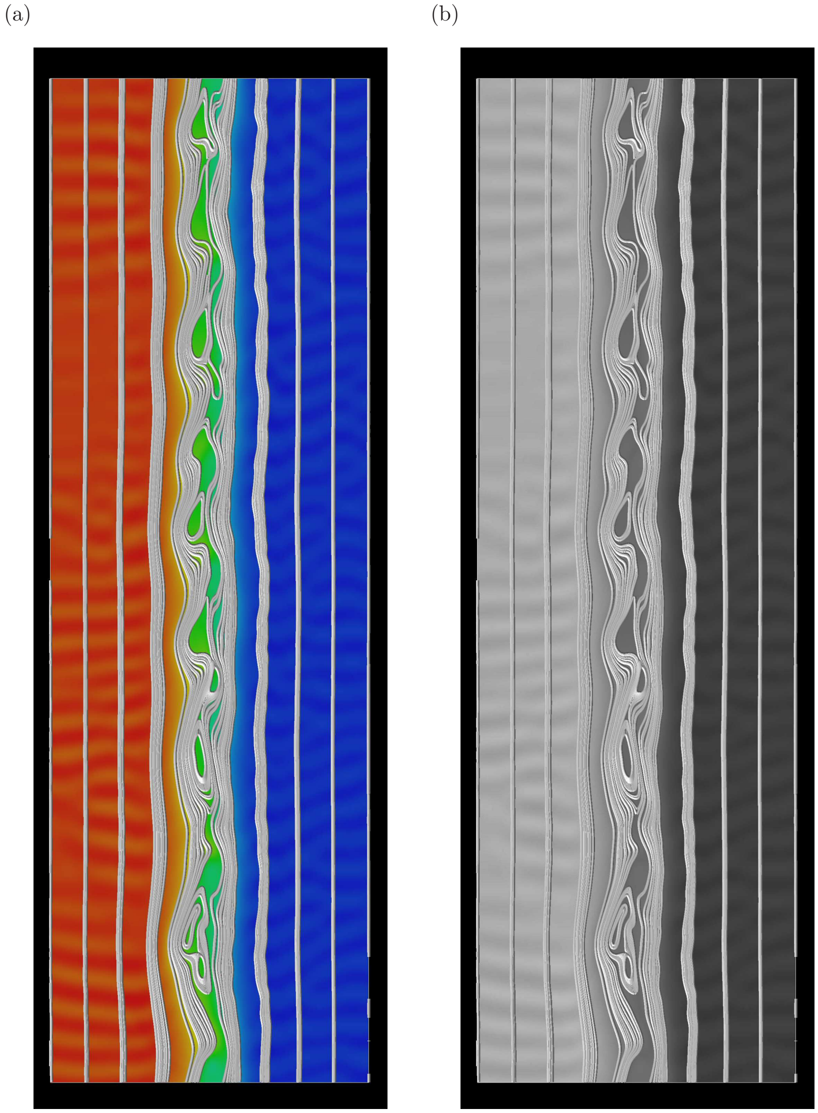

FIG. 3. (a) A color map of the mass density and 2D magnetic field lines in run 2, and (b) magnification of (a) in black and white for the printed version.

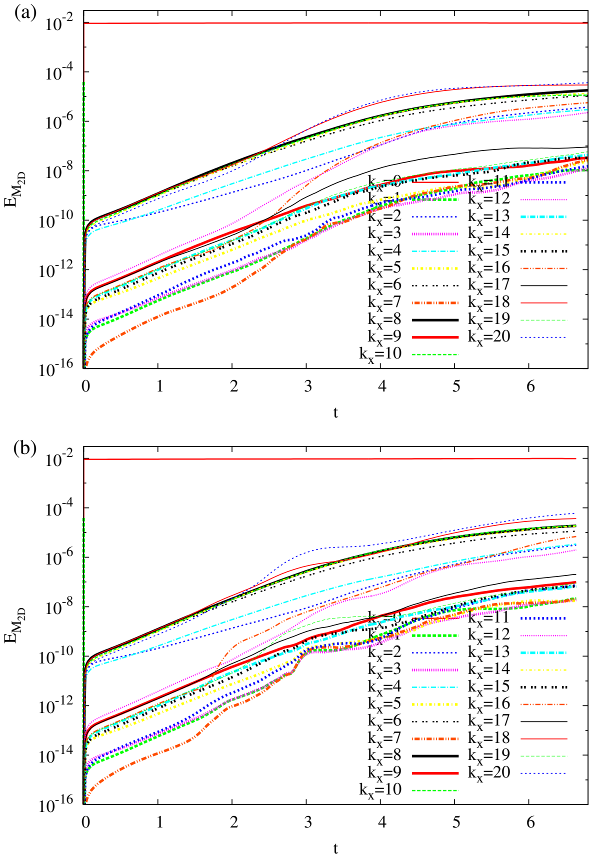

FIG. 4. Fourier energy growth of the magnetic field in (a) run 1 and (b) run 2.

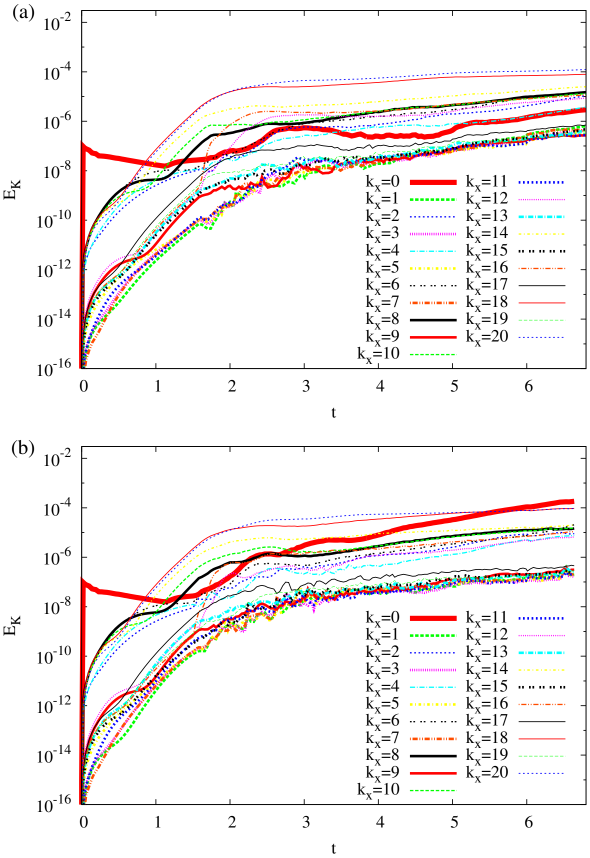

FIG. 5. Fourier energy growth of the velocity field in (a) run 1 and (b) run 2.

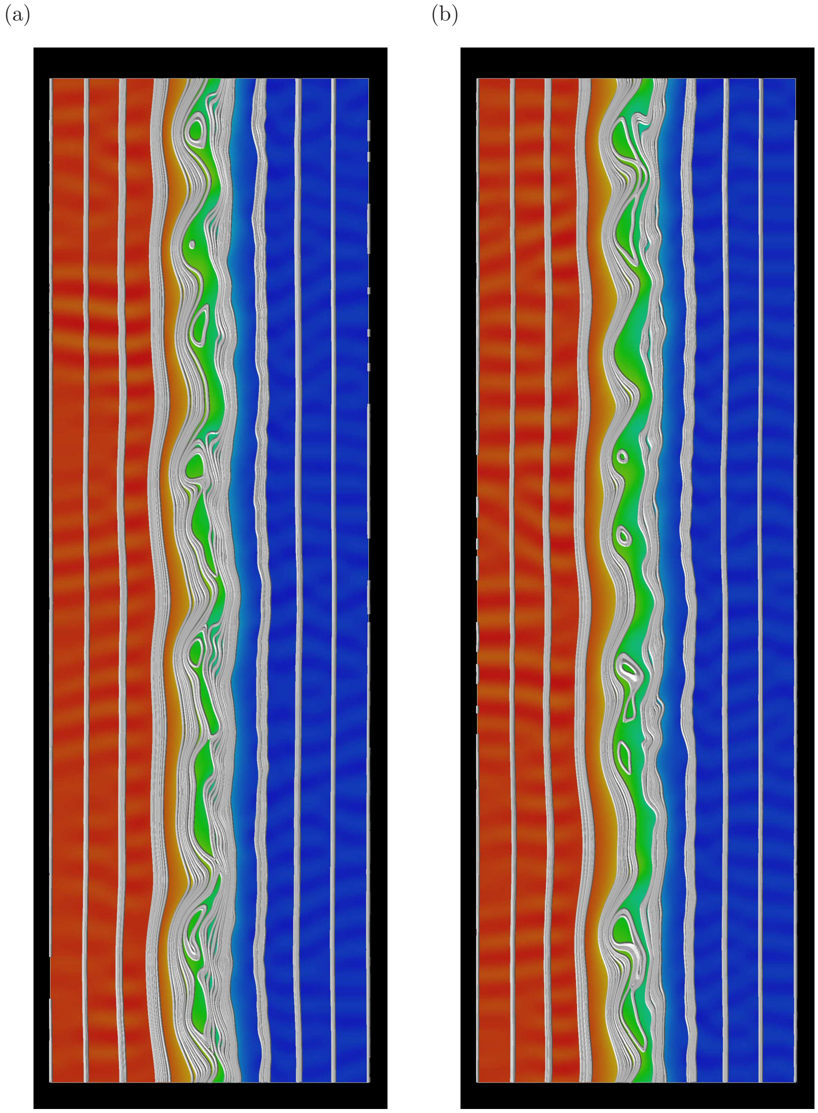

FIG. 6. A color map of the mass density and 2D magnetic field lines in (a) run 3 and (b) run 4. The mass density is larger (or smaller) for a darker (or brighter) color.

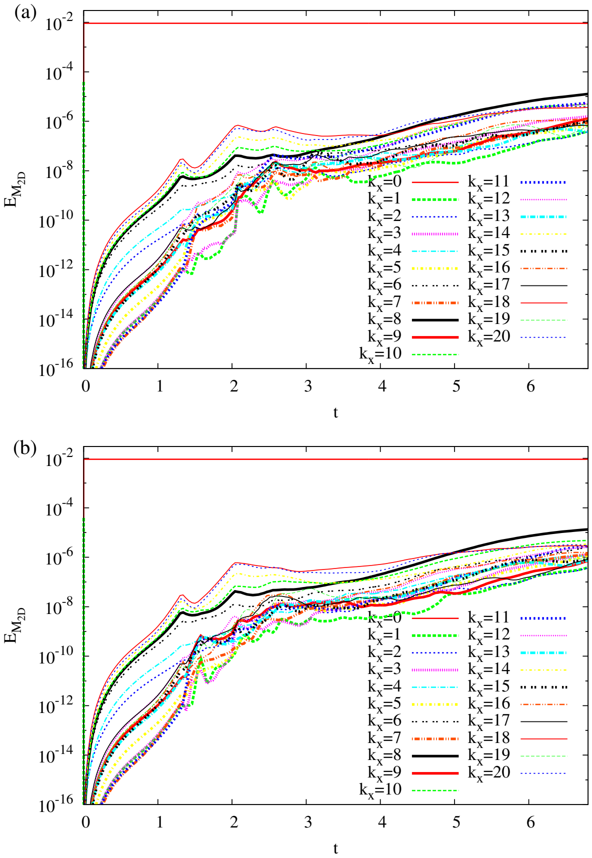

FIG. 7. Fourier energy growth of the magnetic field in (a) run 3 and (b) run4.

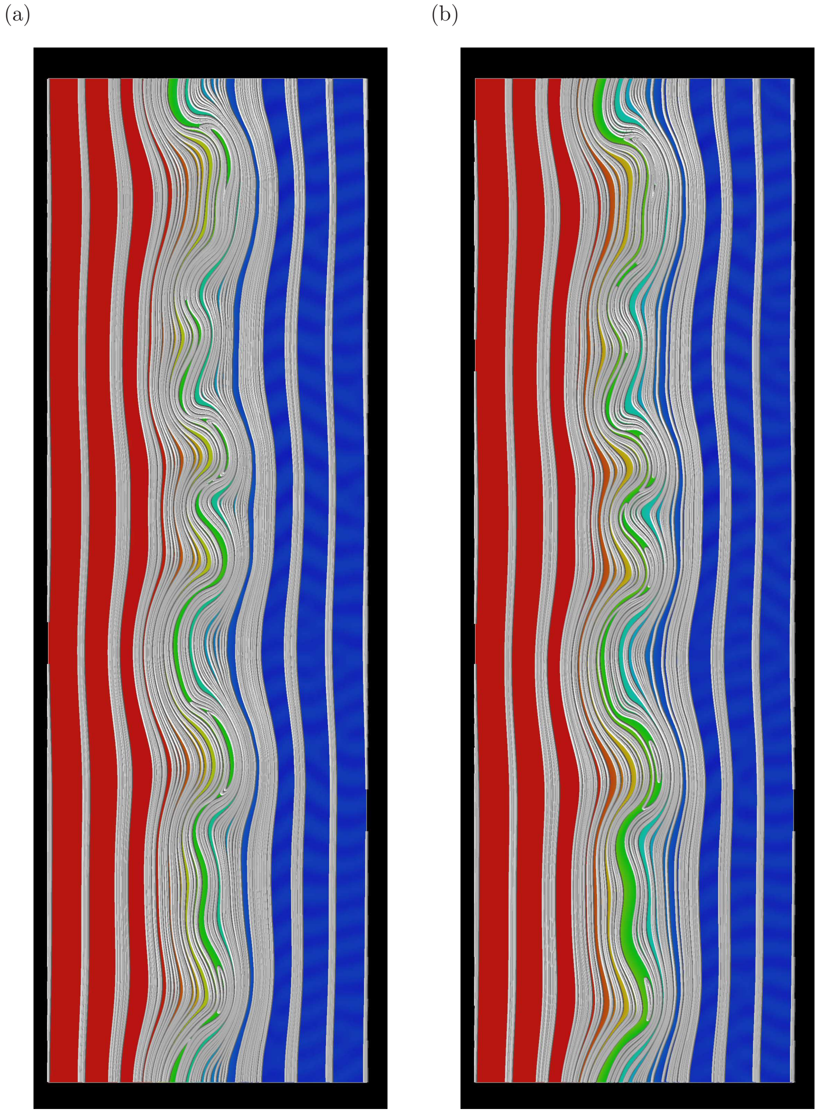

FIG. 8. A color map of the mass density and 2D magnetic field lines in (a) run 5 and (b) run 7. The mass density is larger (or smaller) for a darker (or brighter) color.

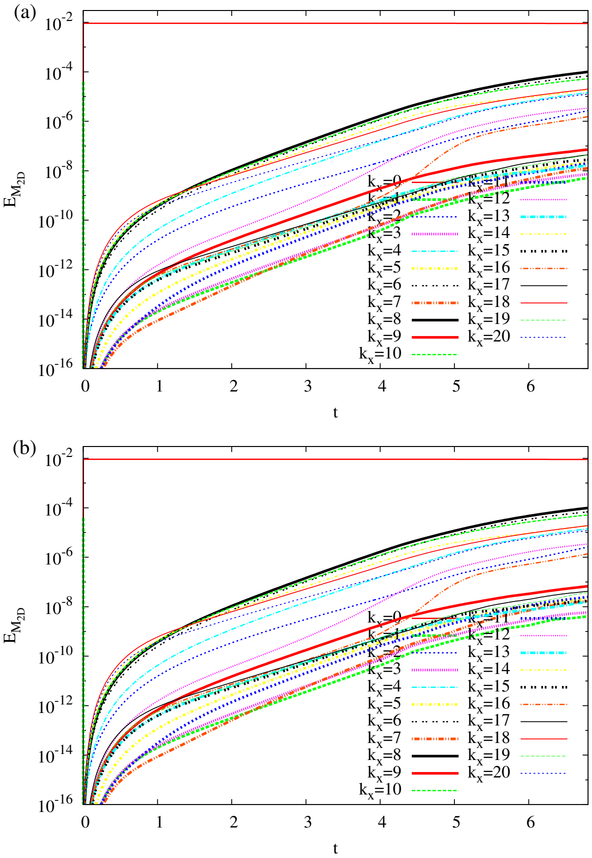

FIG. 9. Fourier energy growth of the magnetic field in (a) run 5 and (b) run 7.

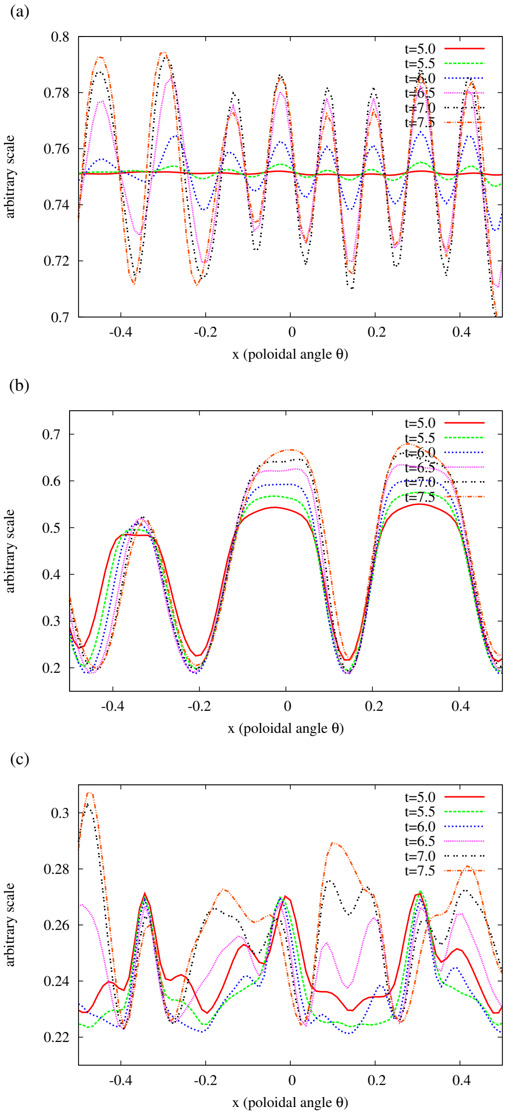

FIG. 10. Time variation of the mass density of run 1 at (a)$y = 0.25$, (b)$y = 0$, and (c)$y = -0.25$.

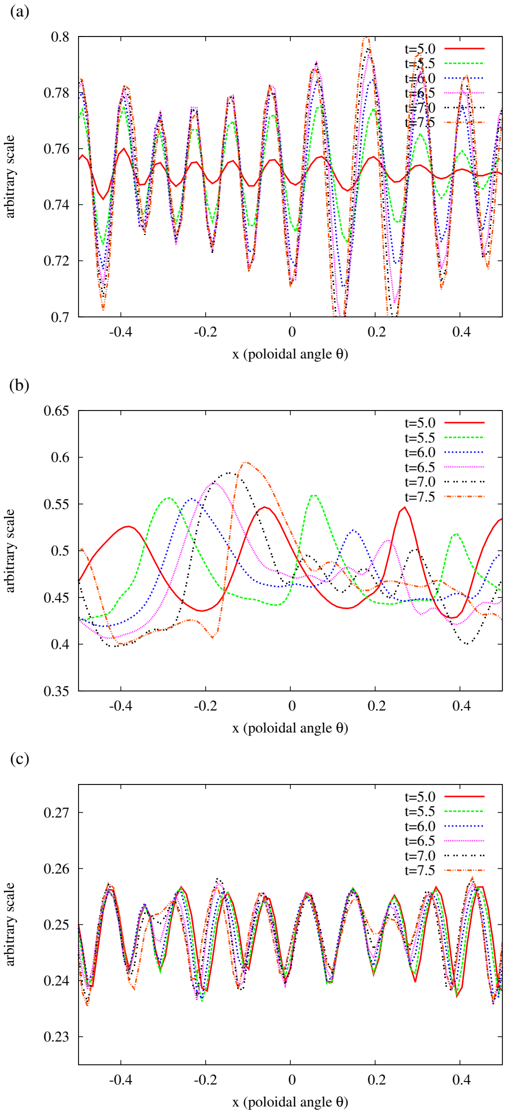

FIG. 11. Time variation of the mass density of run 2 at (a)$y = 0.25$, (b)$y = 0$, and (c)$y = -0.25$.

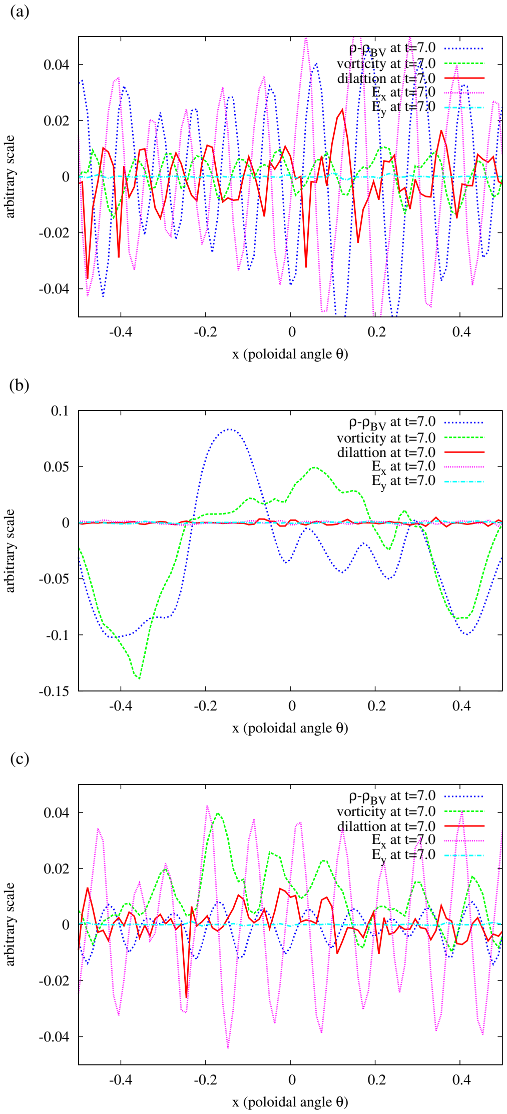

FIG. 12. The mass density, dilatation, vorticity, and electric field components of run 2 at (a)$y = 0.25$, (b)$y = 0$, and (c)$y = -0.25$.

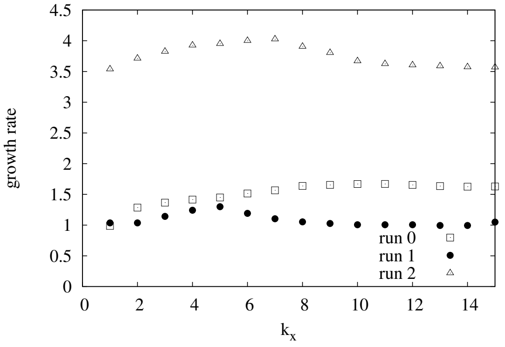

FIG. 13. The linear growth rate in the linear computation corresponding to run 0 (box), run 1 (filled circle), and run 2 (triangle).

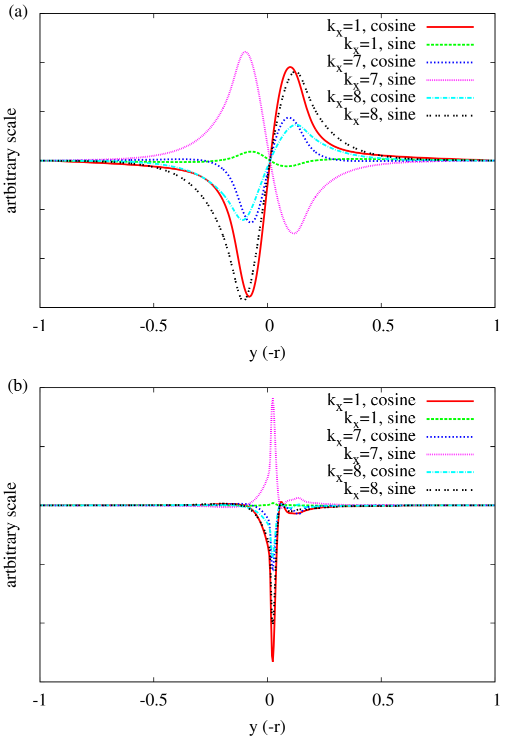

FIG. 14. The cosine and sine parts of the Fourier coefficients of $\widetilde{b}_2$ as the function of the y in the linear computations corresponding to (a) run 0, and (b) run 1, and (c) run 2.

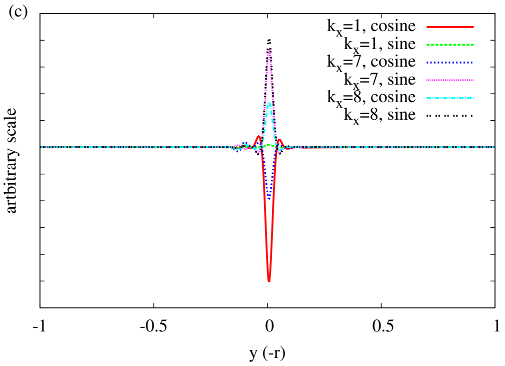

FIG. 14. The cosine and sine parts of the Fourier coefficients of $\widetilde{b}_2$ as the function of the y in the linear computations corresponding to (a) run 0, and (b) run 1, and (c) run 2.

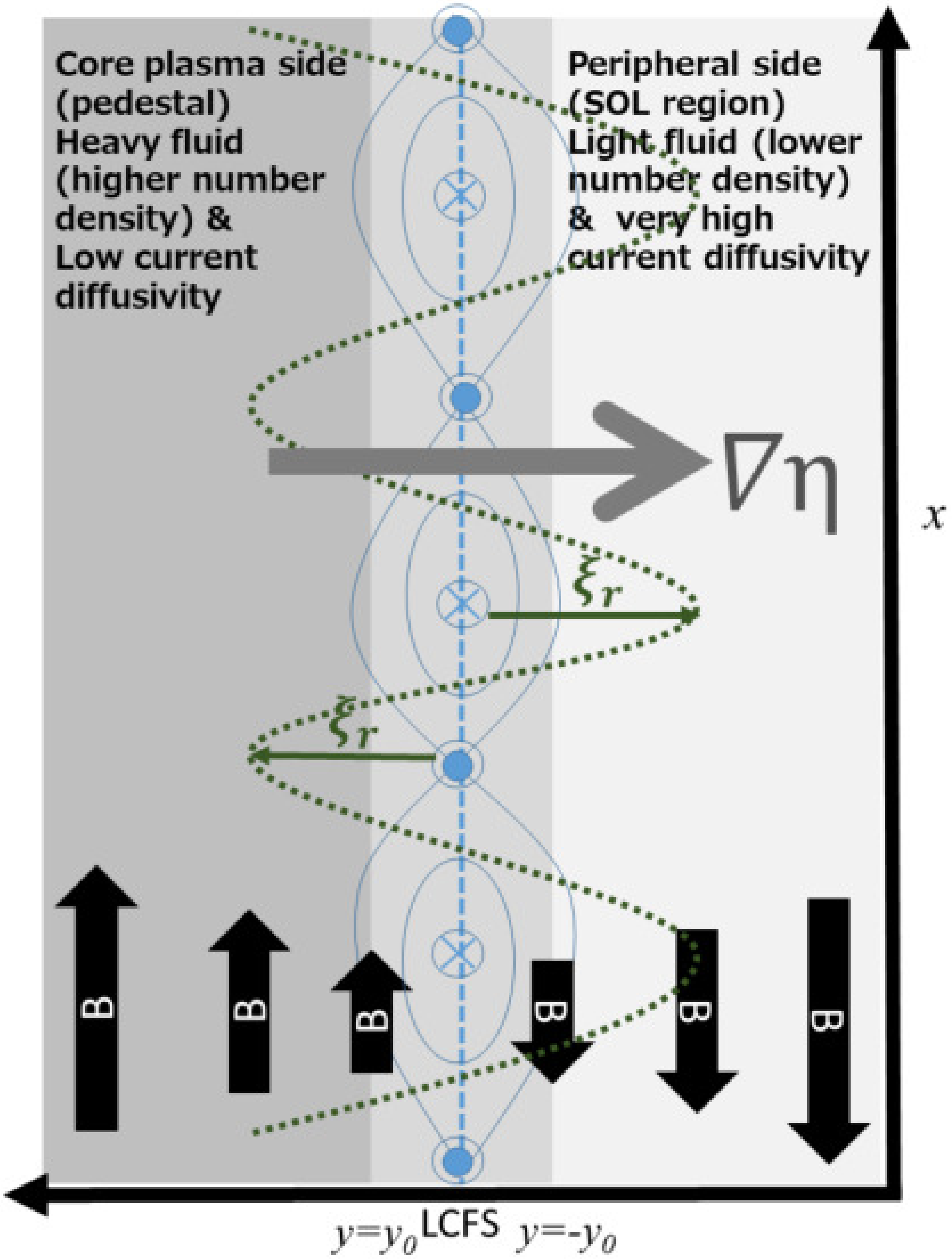
Core plasma side (pedestal) Heavy fluid (higher number density) & Low current diffusivity
Peripheral side (SOL region) Light fluid (lower number density) & very high current diffusivity
$\nabla\eta$
x
ξ_r
ξ_r
B
B
B
B
B
B
$y=y_0$
LCFS
$y=-y_0$

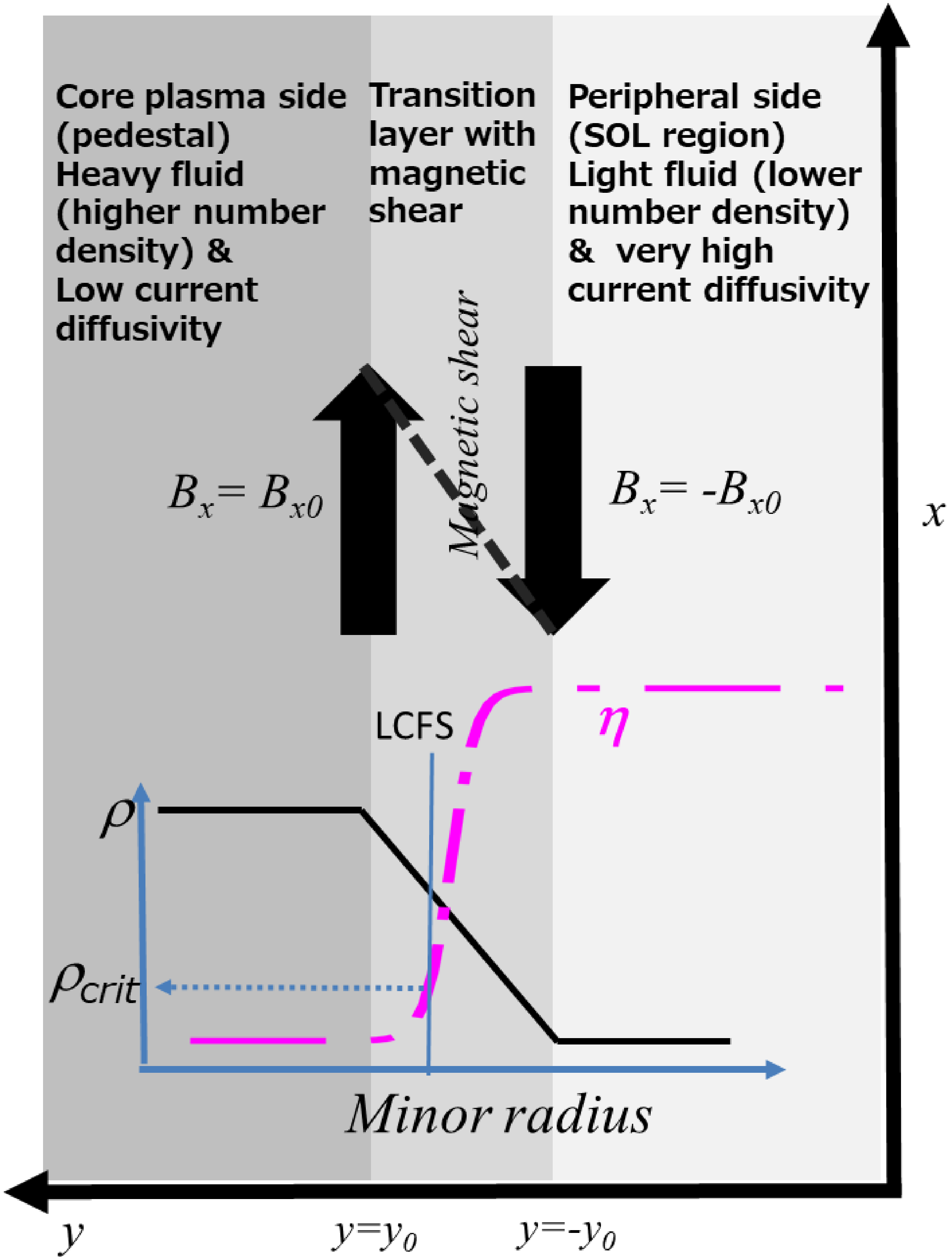
Core plasma side (pedestal) Heavy fluid (higher number density) & Low current diffusivity
Transition layer with magnetic shear
Peripheral side (SOL region) Light fluid (lower number density) & very high current diffusivity
$B_x = B_{x0}$
Magnetic shear
$B_x = -B_{x0}$
x
LCFS
η
ρ
ρ_{crit}
Minor radius
y
$y=y_0$
$y=-y_0$

PLEASE CITE THIS ARTICLE AS DOI: 10.1063/5.0106785

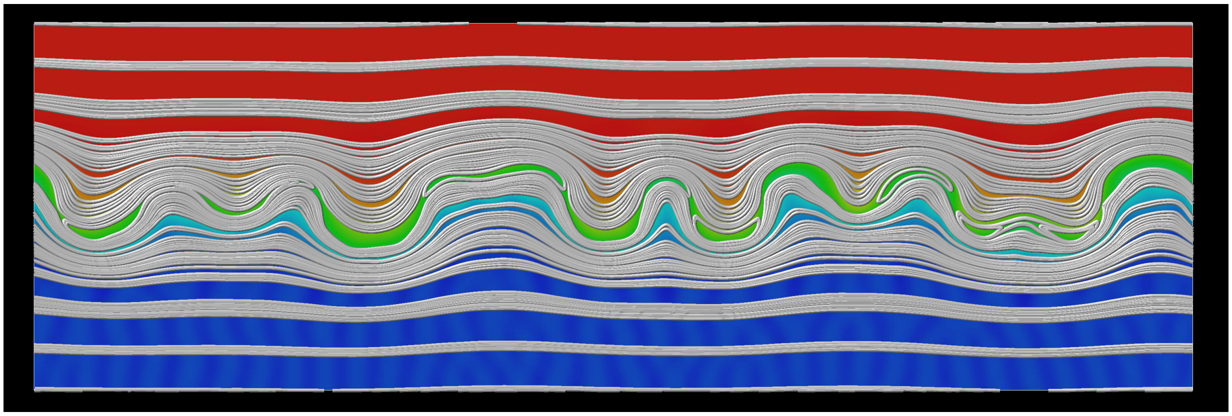

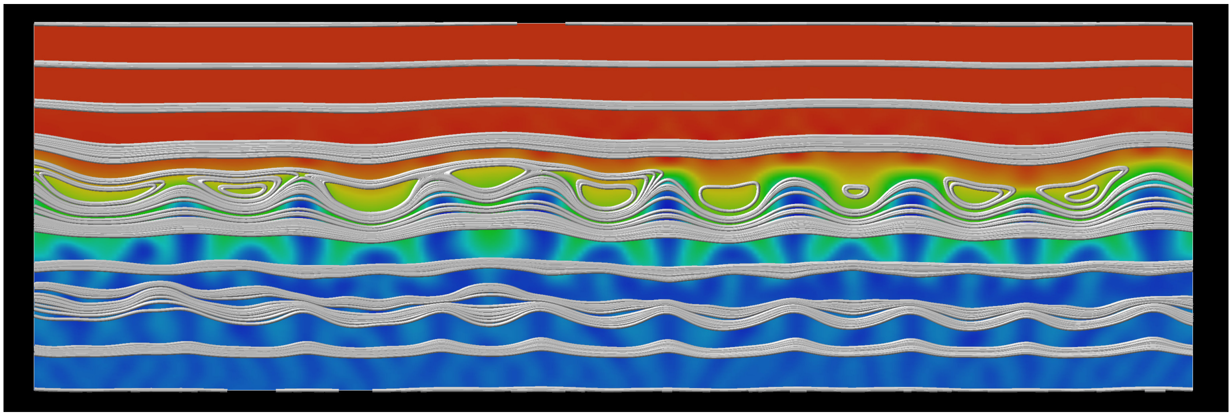

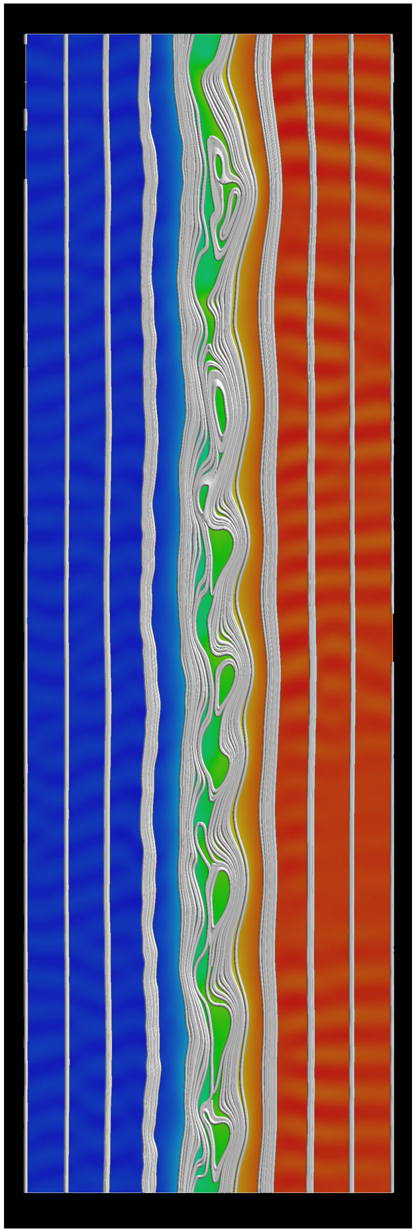

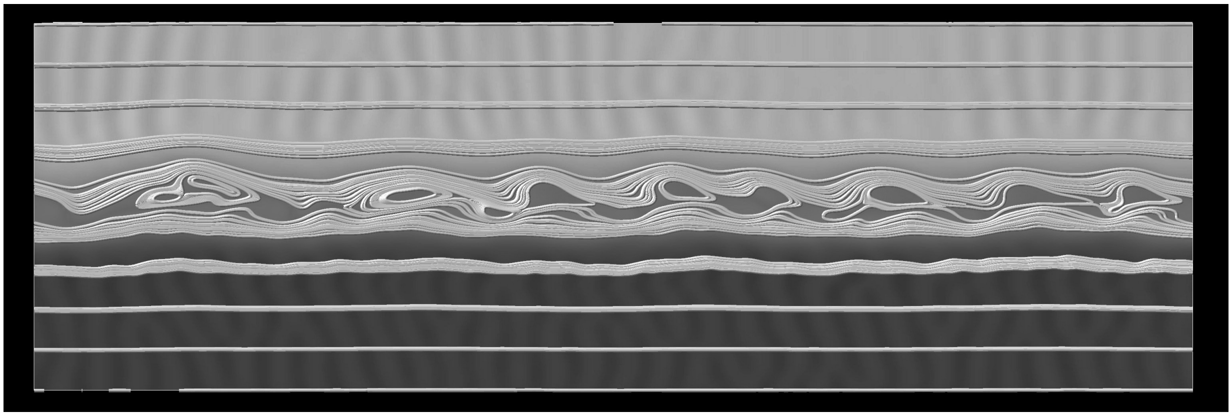

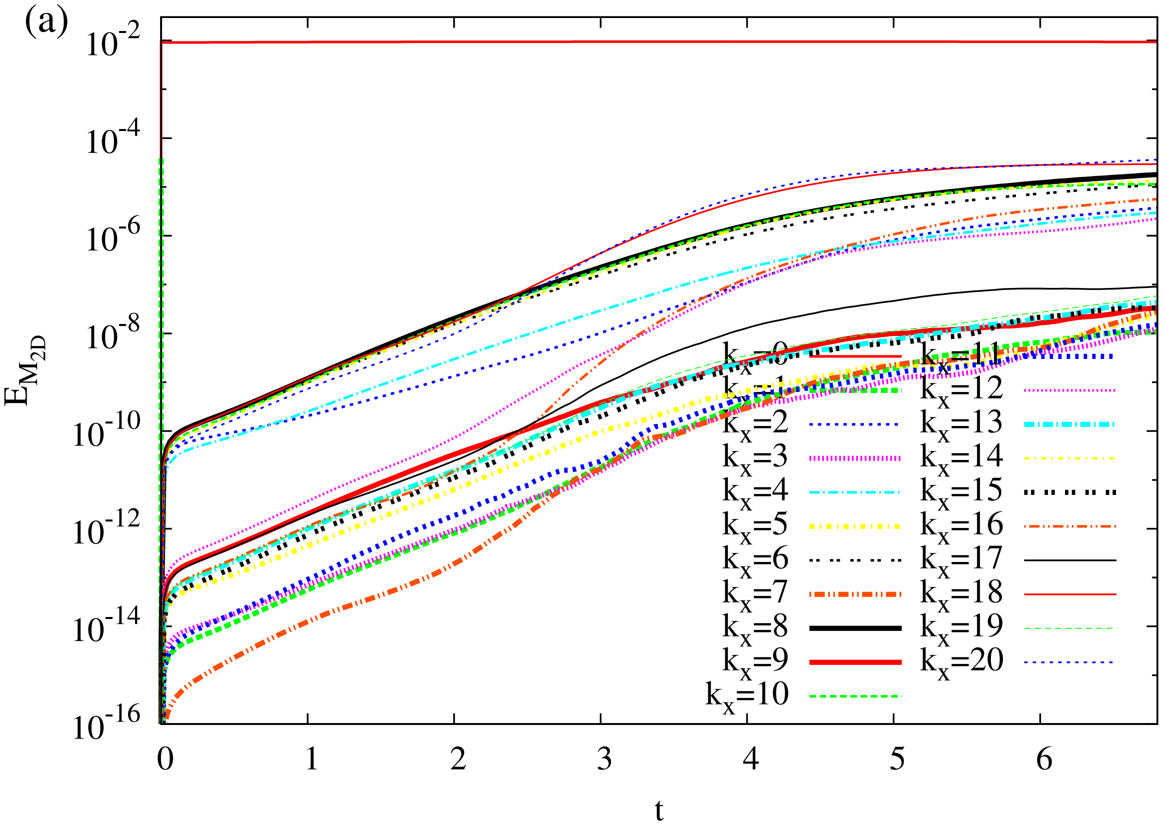
(a)
$E_{M_{2D}}$
10^{-2}
10^{-4}
10^{-6}
10^{-8}
10^{-10}
10^{-12}
10^{-14}
10^{-16}
0
1
2
3
4
5
6
t
$k_x=0$
$k_x=1$
$k_x=2$
$k_x=3$
$k_x=4$
$k_x=5$
$k_x=6$
$k_x=7$
$k_x=8$
$k_x=9$
$k_x=10$
$k_x=11$
$k_x=12$
$k_x=13$
$k_x=14$
$k_x=15$
$k_x=16$
$k_x=17$
$k_x=18$
$k_x=19$
$k_x=20$

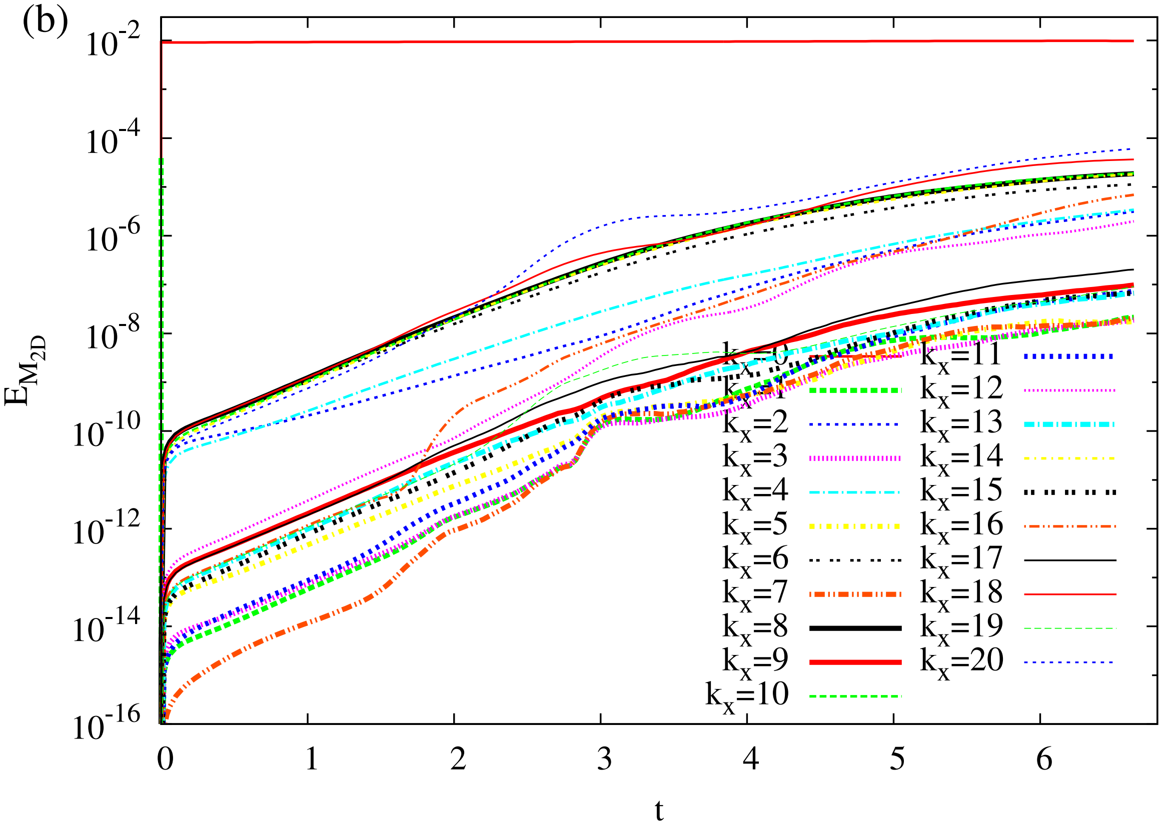
(b)
$E_{M_{2D}}$
t
10^{-2}
10^{-4}
10^{-6}
10^{-8}
10^{-10}
10^{-12}
10^{-14}
10^{-16}
0
1
2
3
4
5
6
$k_x=0$
$k_x=1$
$k_x=2$
$k_x=3$
$k_x=4$
$k_x=5$
$k_x=6$
$k_x=7$
$k_x=8$
$k_x=9$
$k_x=10$
$k_x=11$
$k_x=12$
$k_x=13$
$k_x=14$
$k_x=15$
$k_x=16$
$k_x=17$
$k_x=18$
$k_x=19$
$k_x=20$

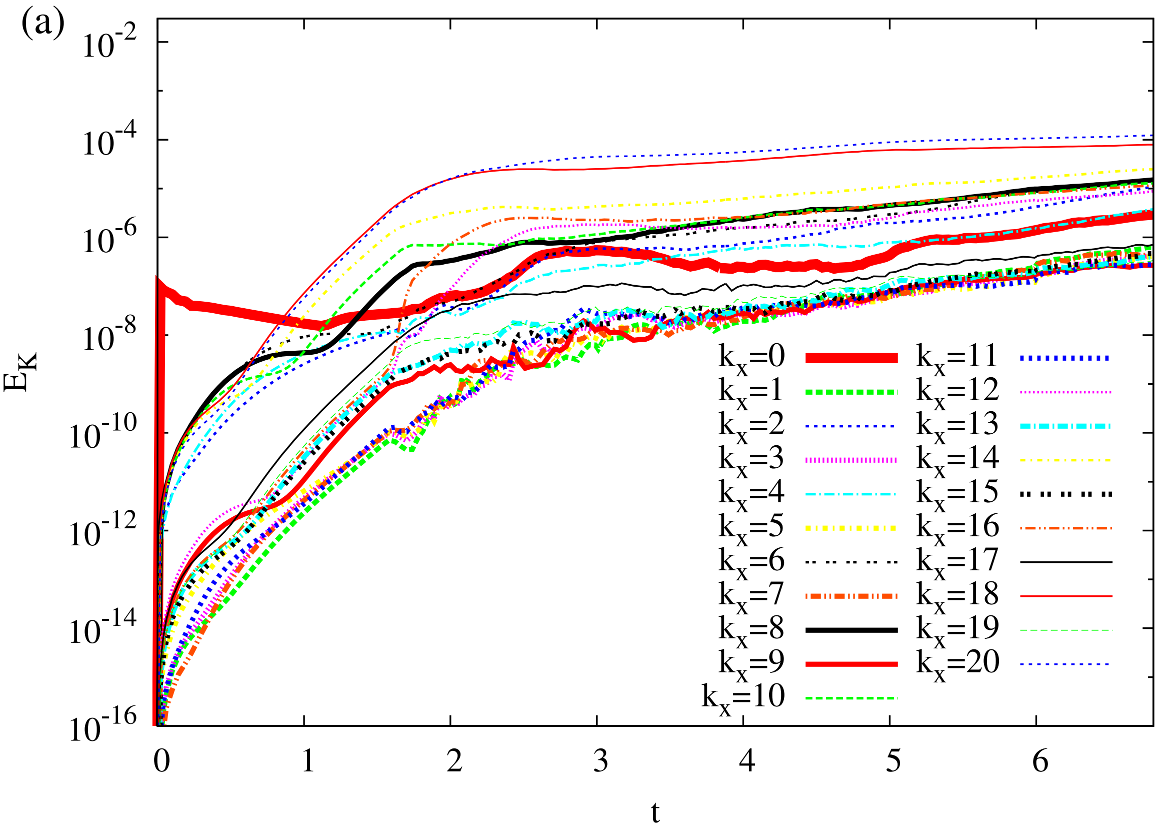
(a)
E_K
t
10^-2
10^-4
10^-6
10^-8
10^-10
10^-12
10^-14
10^-16
0
1
2
3
4
5
6
k_x=0
k_x=1
k_x=2
k_x=3
k_x=4
k_x=5
k_x=6
k_x=7
k_x=8
k_x=9
k_x=10
k_x=11
k_x=12
k_x=13
k_x=14
k_x=15
k_x=16
k_x=17
k_x=18
k_x=19
k_x=20

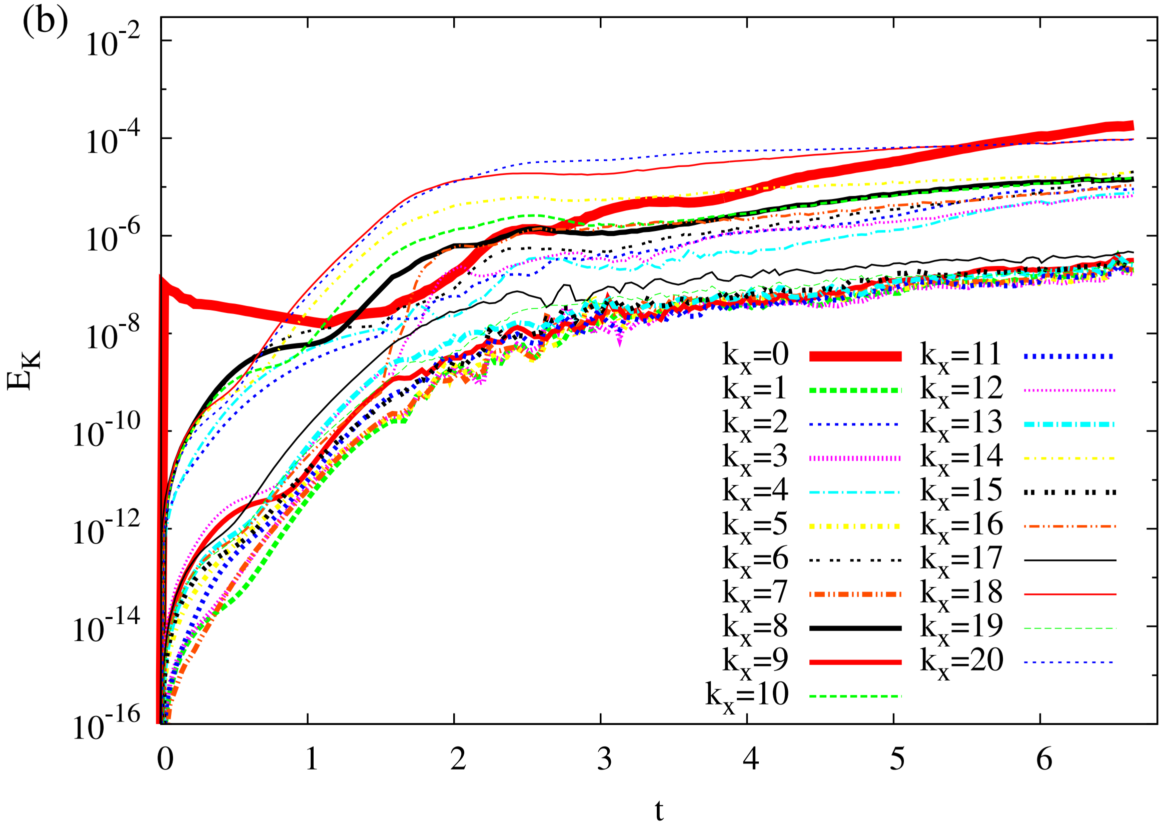
(b)
E_K
t
10^{-2}
10^{-4}
10^{-6}
10^{-8}
10^{-10}
10^{-12}
10^{-14}
10^{-16}
0
1
2
3
4
5
6
$k_x=0$
$k_x=1$
$k_x=2$
$k_x=3$
$k_x=4$
$k_x=5$
$k_x=6$
$k_x=7$
$k_x=8$
$k_x=9$
$k_x=10$
$k_x=11$
$k_x=12$
$k_x=13$
$k_x=14$
$k_x=15$
$k_x=16$
$k_x=17$
$k_x=18$
$k_x=19$
$k_x=20$

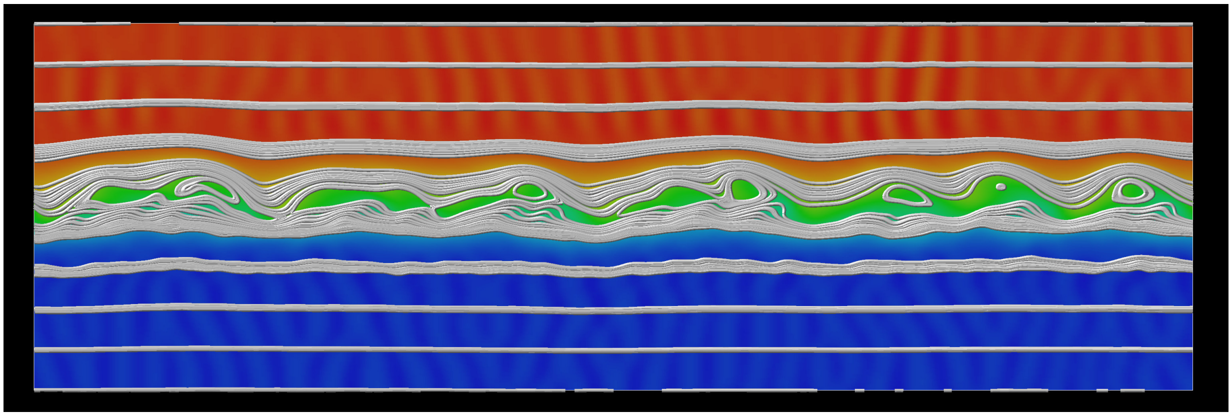

AIP
Publishing

Physics of Plasmas

ACCEPTED MANUSCRIPT

This is the author's peer reviewed, accepted manuscript. However, the online version of record will be different from this version once it has been copyedited and typeset.

PLEASE CITE THIS ARTICLE AS DOI: 10.1063/5.0106785

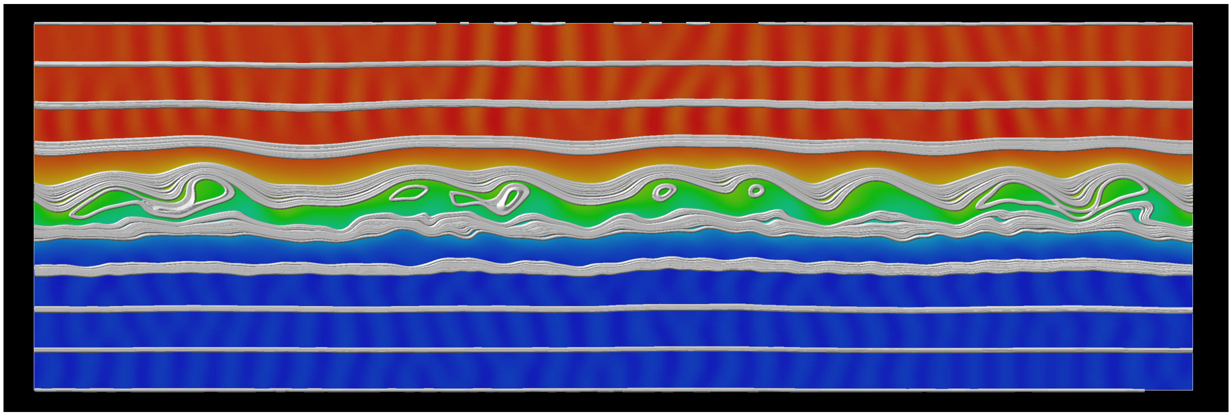

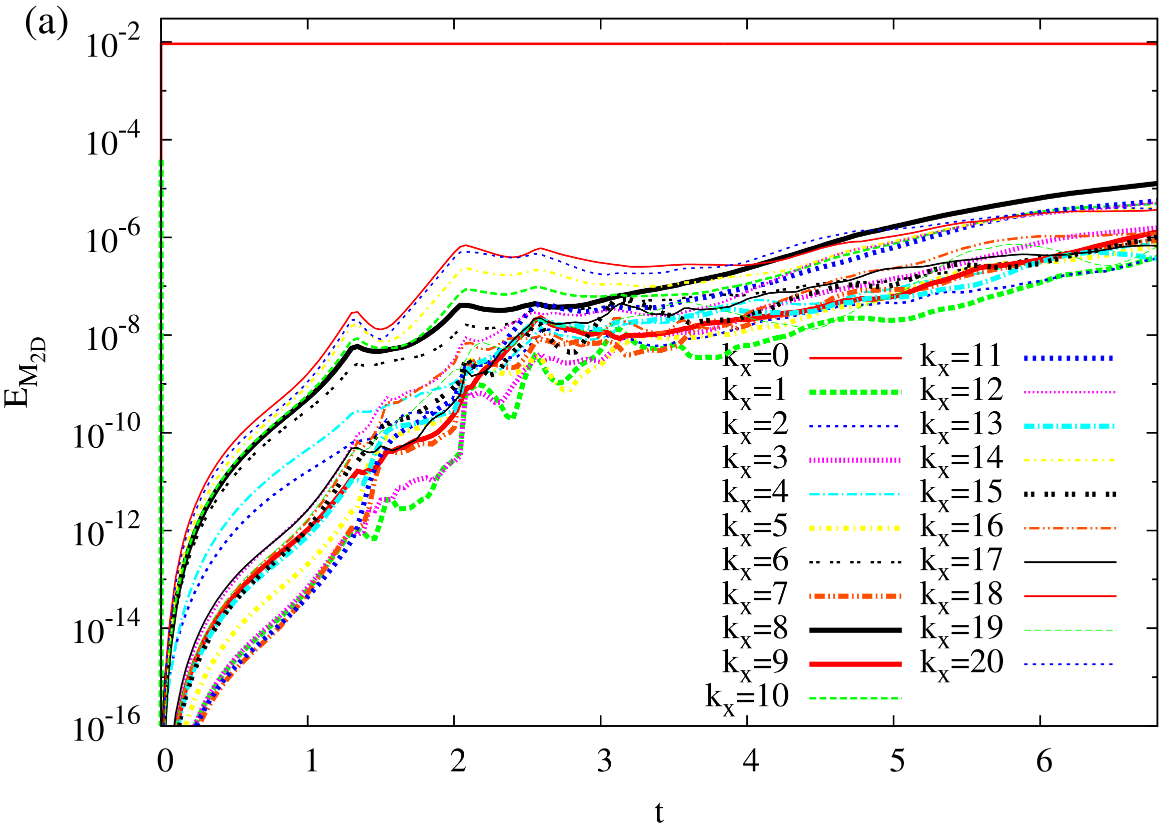
(a)
$E_{M_{2D}}$
10^{-2}
10^{-4}
10^{-6}
10^{-8}
10^{-10}
10^{-12}
10^{-14}
10^{-16}
0
1
2
3
4
5
6
t
k_x=0
k_x=1
k_x=2
k_x=3
k_x=4
k_x=5
k_x=6
k_x=7
k_x=8
k_x=9
k_x=10
k_x=11
k_x=12
k_x=13
k_x=14
k_x=15
k_x=16
k_x=17
k_x=18
k_x=19
k_x=20

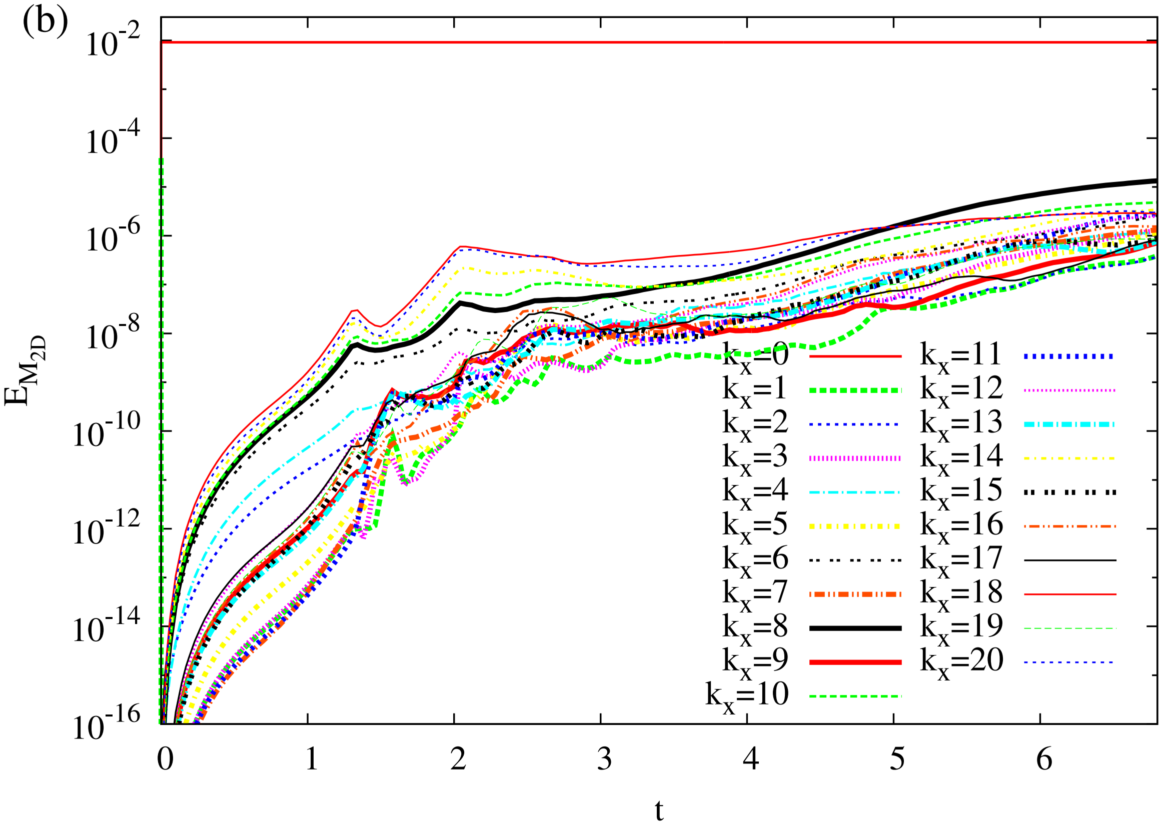
(b)
$E_{M_{2D}}$
10^{-2}
10^{-4}
10^{-6}
10^{-8}
10^{-10}
10^{-12}
10^{-14}
10^{-16}
0
1
2
3
4
5
6
t
k_x=0
k_x=1
k_x=2
k_x=3
k_x=4
k_x=5
k_x=6
k_x=7
k_x=8
k_x=9
k_x=10
k_x=11
k_x=12
k_x=13
k_x=14
k_x=15
k_x=16
k_x=17
k_x=18
k_x=19
k_x=20

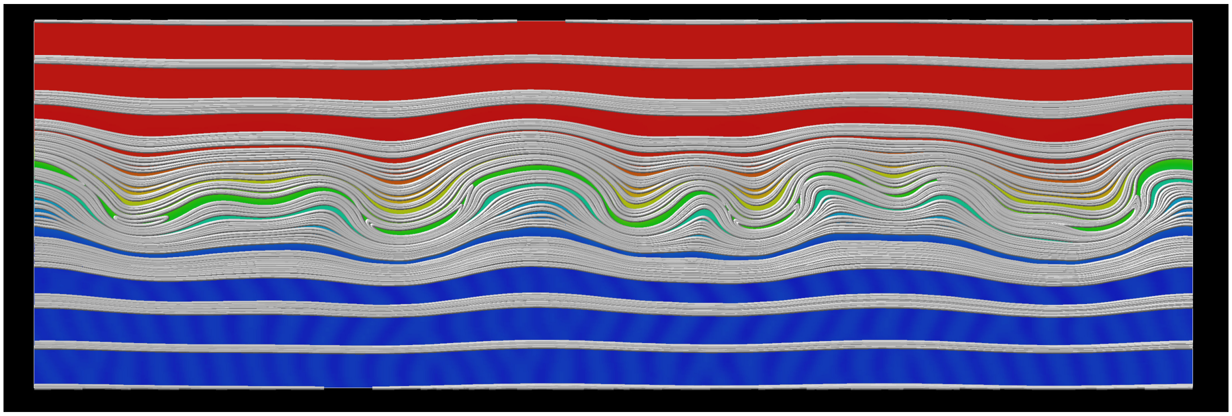

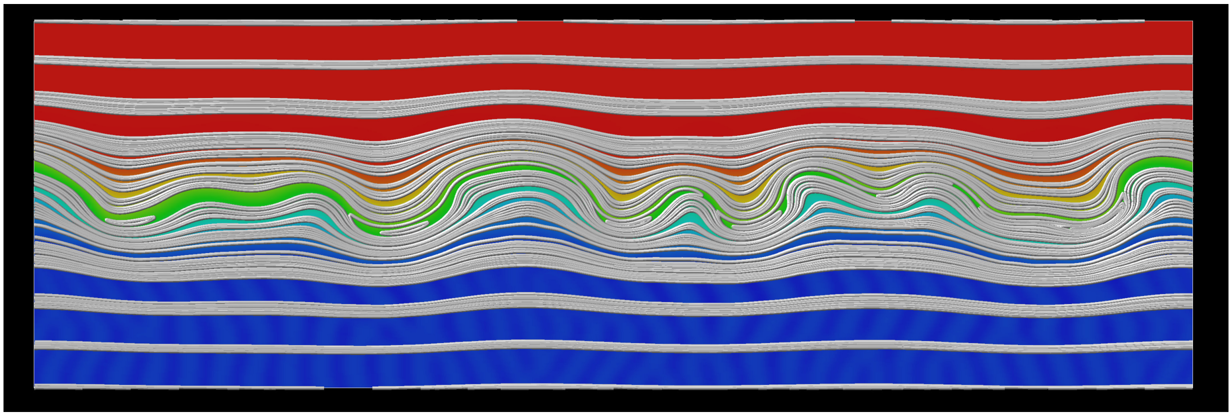

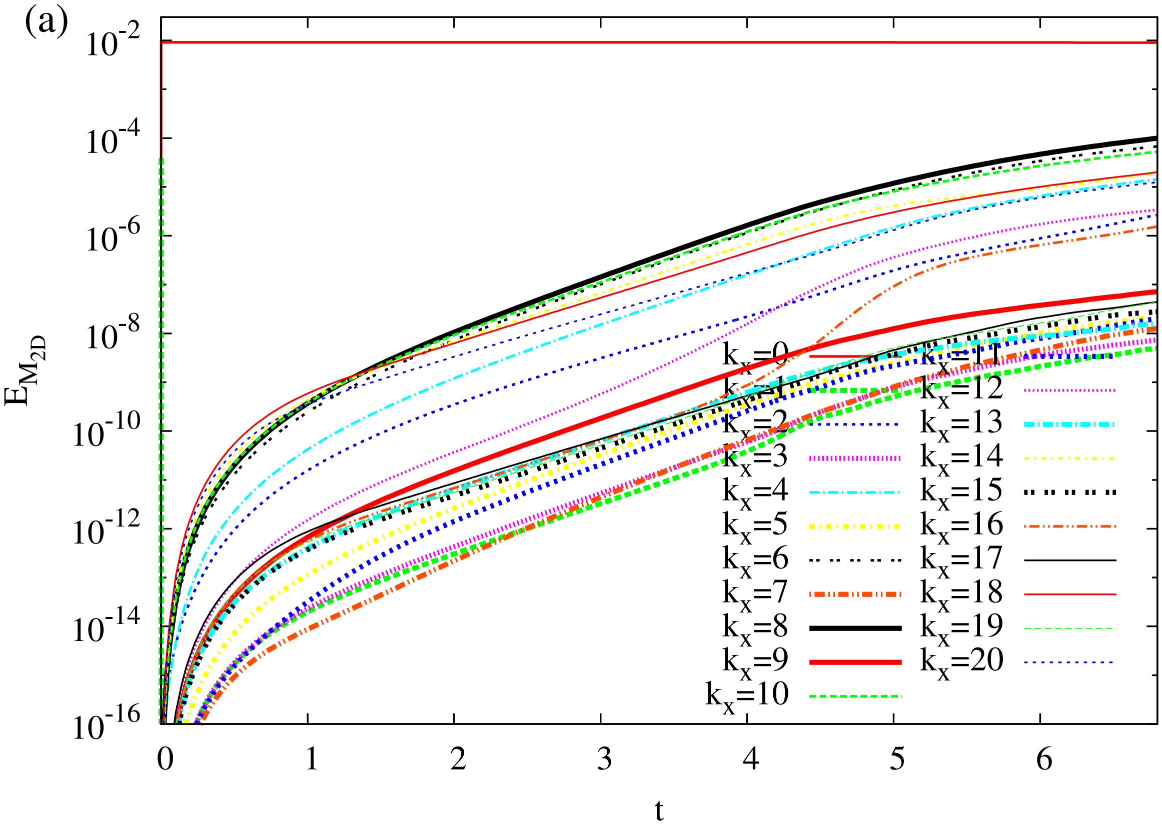
(a)
$E_{M_{2D}}$
10^{-2}
10^{-4}
10^{-6}
10^{-8}
10^{-10}
10^{-12}
10^{-14}
10^{-16}
0
1
2
3
4
5
6
t
$k_x=0$
$k_x=1$
$k_x=2$
$k_x=3$
$k_x=4$
$k_x=5$
$k_x=6$
$k_x=7$
$k_x=8$
$k_x=9$
$k_x=10$
$k_x=11$
$k_x=12$
$k_x=13$
$k_x=14$
$k_x=15$
$k_x=16$
$k_x=17$
$k_x=18$
$k_x=19$
$k_x=20$

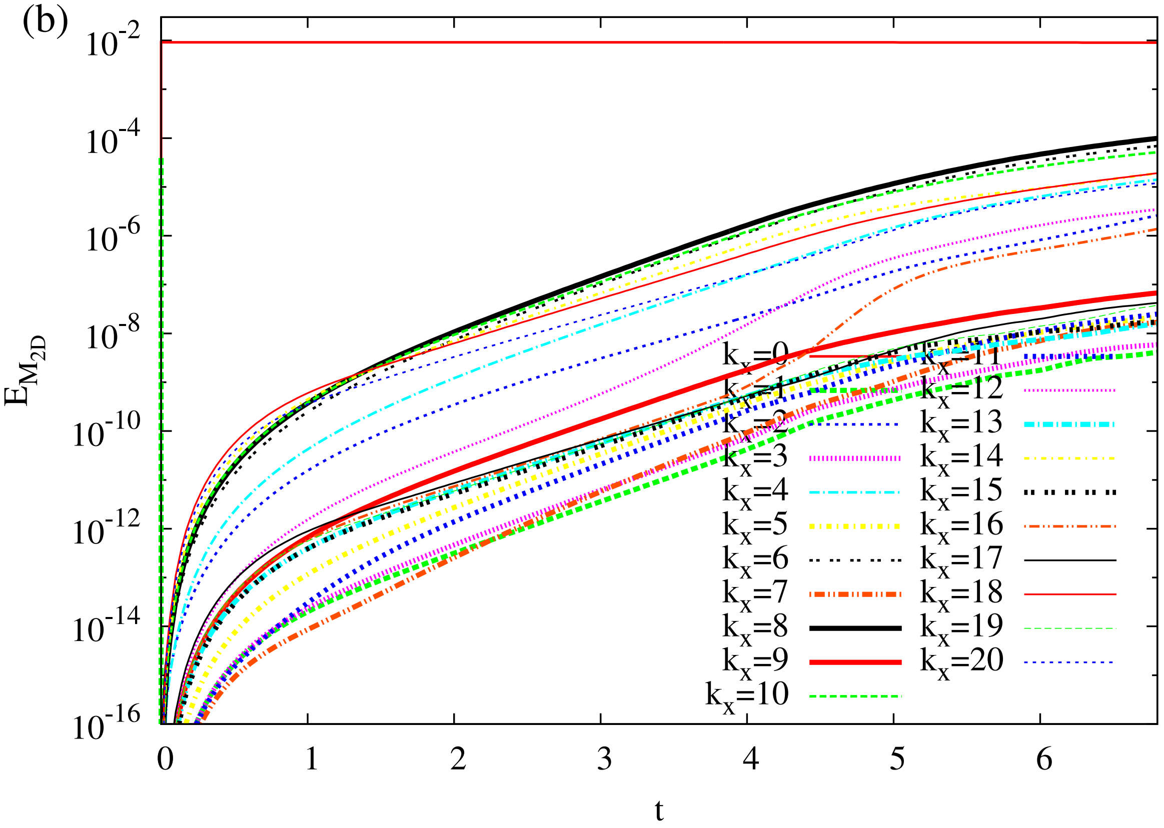
(b)
$E_{M_{2D}}$
t
10^{-2}
10^{-4}
10^{-6}
10^{-8}
10^{-10}
10^{-12}
10^{-14}
10^{-16}
0
1
2
3
4
5
6
k_x=0
k_x=1
k_x=2
k_x=3
k_x=4
k_x=5
k_x=6
k_x=7
k_x=8
k_x=9
k_x=10
k_x=11
k_x=12
k_x=13
k_x=14
k_x=15
k_x=16
k_x=17
k_x=18
k_x=19
k_x=20

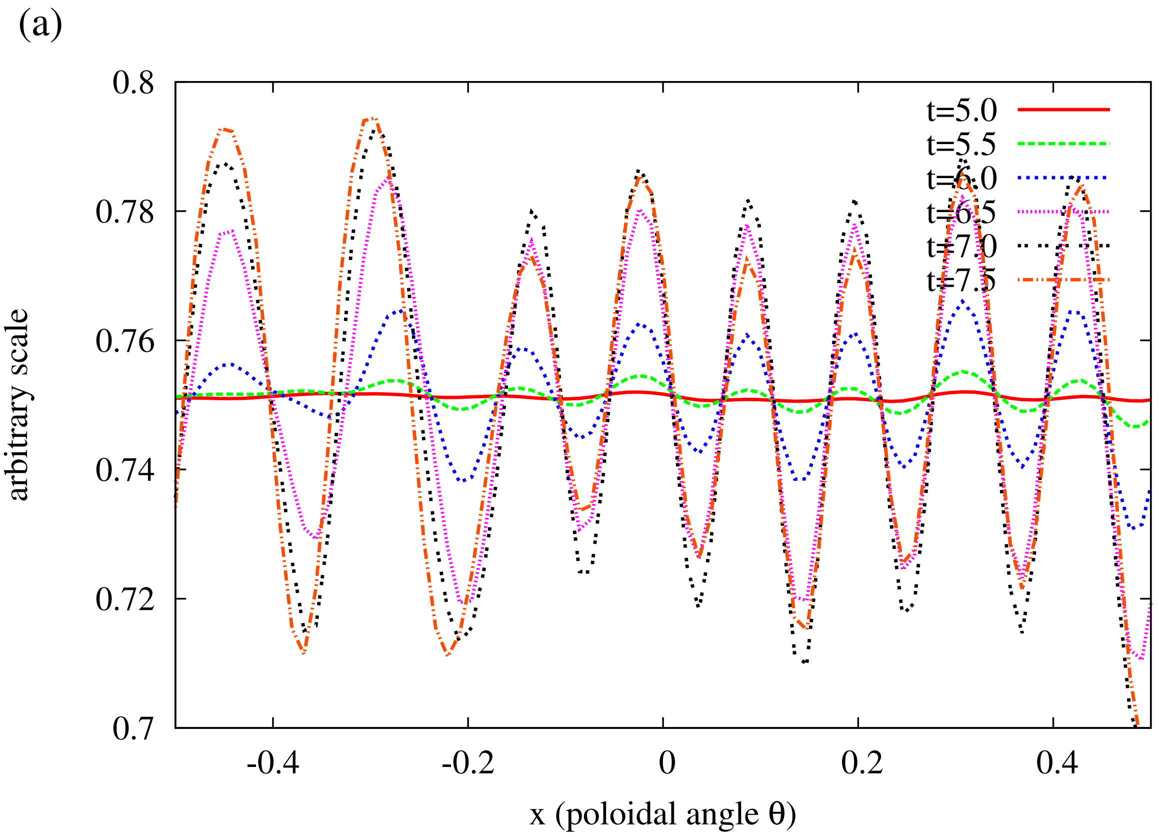
(a)
t=5.0
t=5.5
t=6.0
t=6.5
t=7.0
t=7.5
arbitrary scale
0.8
0.78
0.76
0.74
0.72
0.7
-0.4
-0.2
0
0.2
0.4
x (poloidal angle θ)

AIP
Publishing

Physics of Plasmas

ACCEPTED MANUSCRIPT

This is the author's peer reviewed, accepted manuscript. However, the online version of record will be different from this version once it has been copyedited and typeset.

PLEASE CITE THIS ARTICLE AS DOI: 10.1063/5.0106785

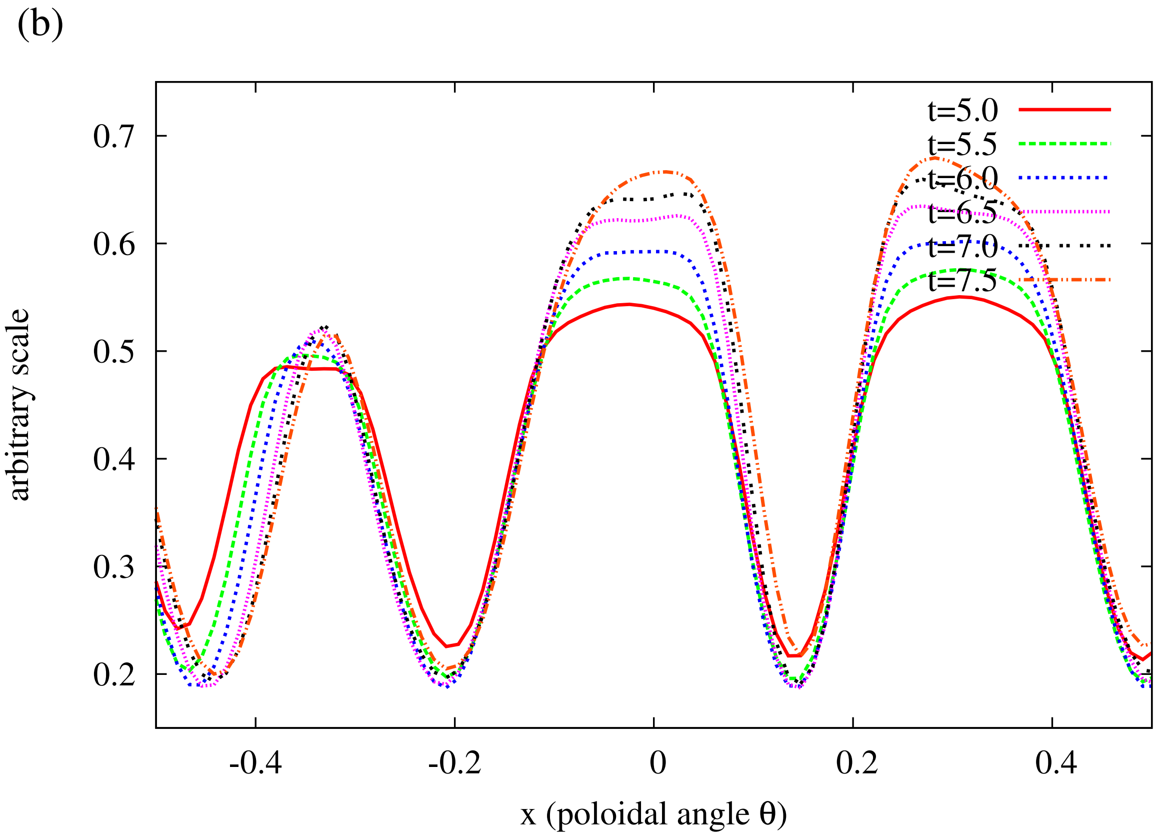

(c)

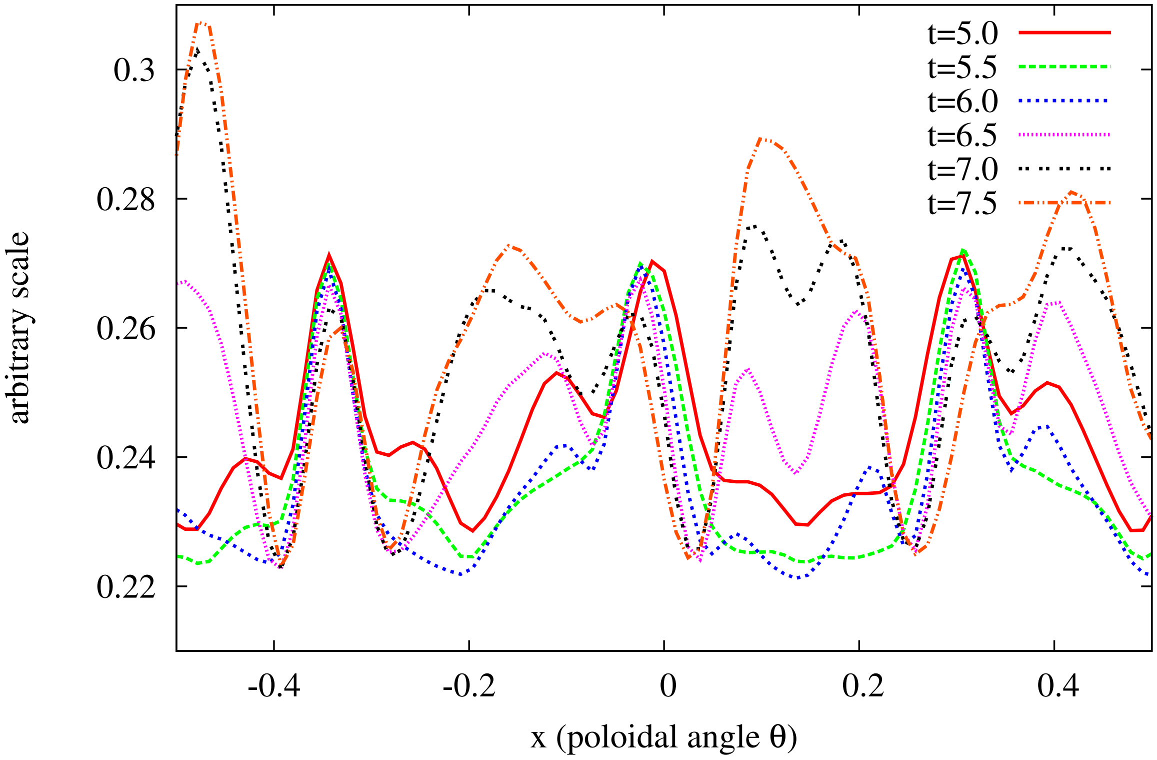
t=5.0
t=5.5
t=6.0
t=6.5
t=7.0
t=7.5
0.3
0.28
0.26
0.24
0.22
arbitrary scale
-0.4
-0.2
0
0.2
0.4
x (poloidal angle θ)

(a)

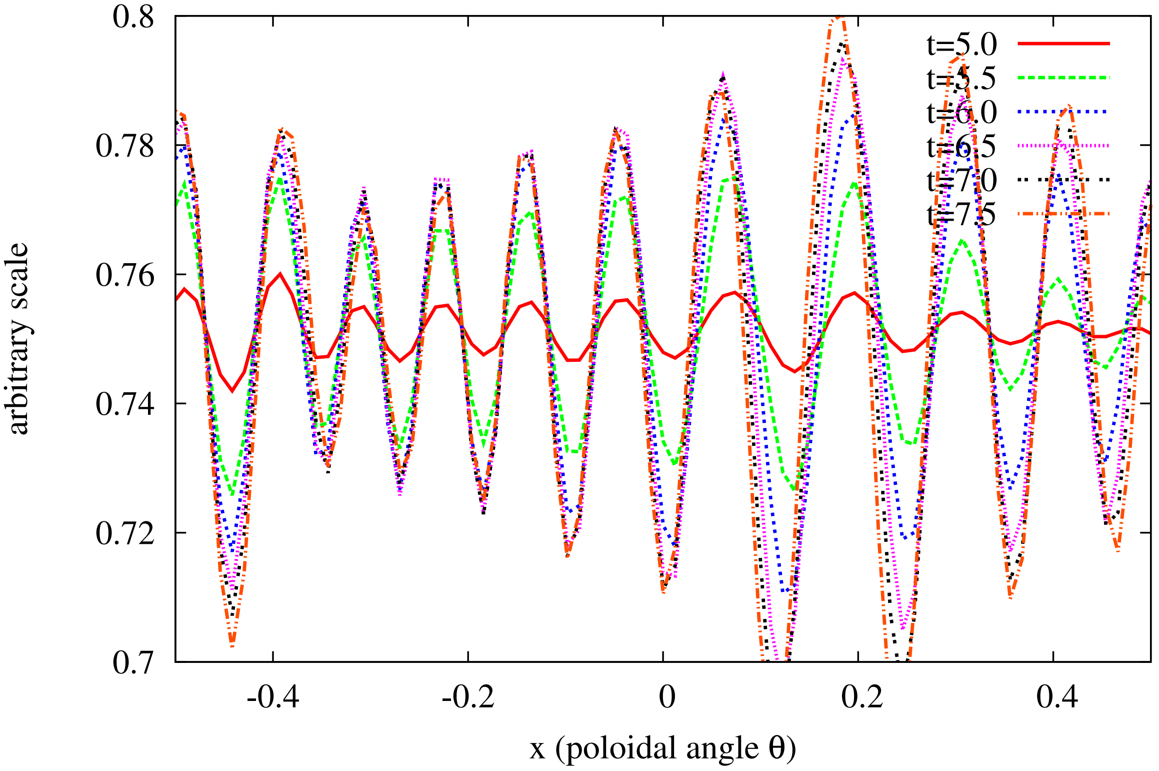
0.8
0.78
0.76
0.74
0.72
0.7
-0.4
-0.2
0
0.2
0.4
arbitrary scale
x (poloidal angle θ)
t=5.0
t=5.5
t=6.0
t=6.5
t=7.0
t=7.5

(b)

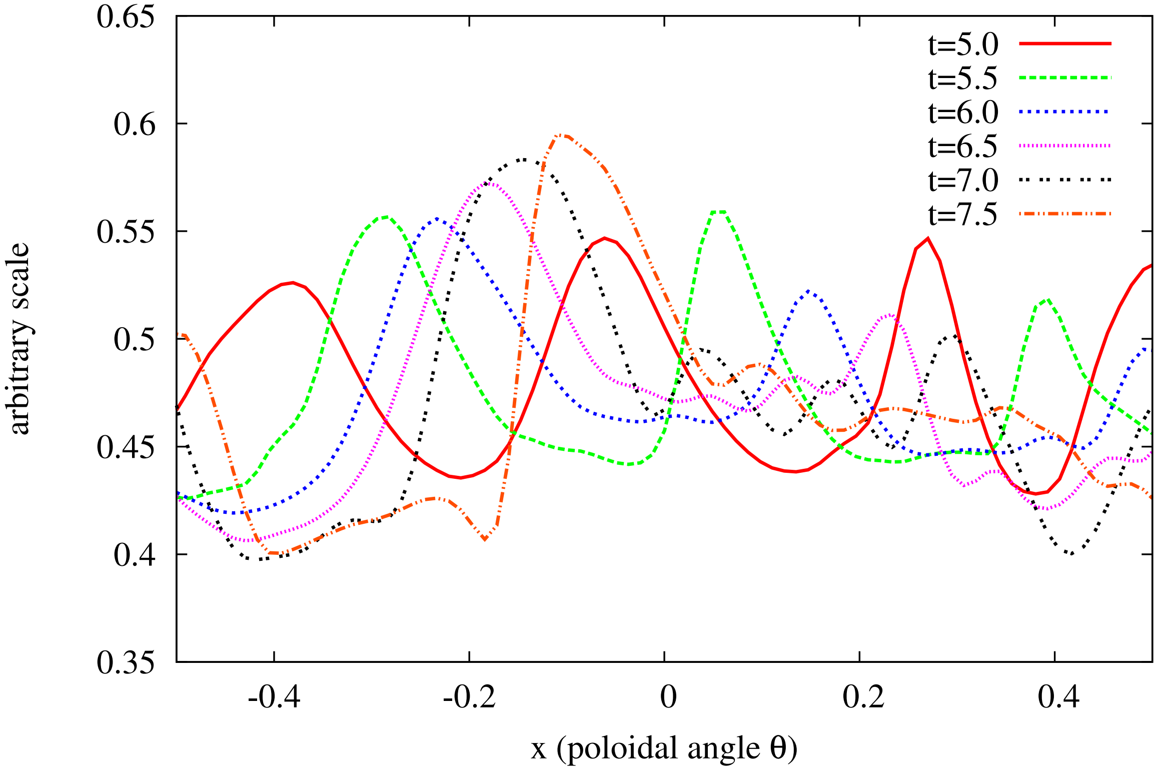
0.65
0.6
0.55
0.5
0.45
0.4
0.35
arbitrary scale
-0.4
-0.2
0
0.2
0.4
x (poloidal angle θ)
t=5.0
t=5.5
t=6.0
t=6.5
t=7.0
t=7.5

(c)

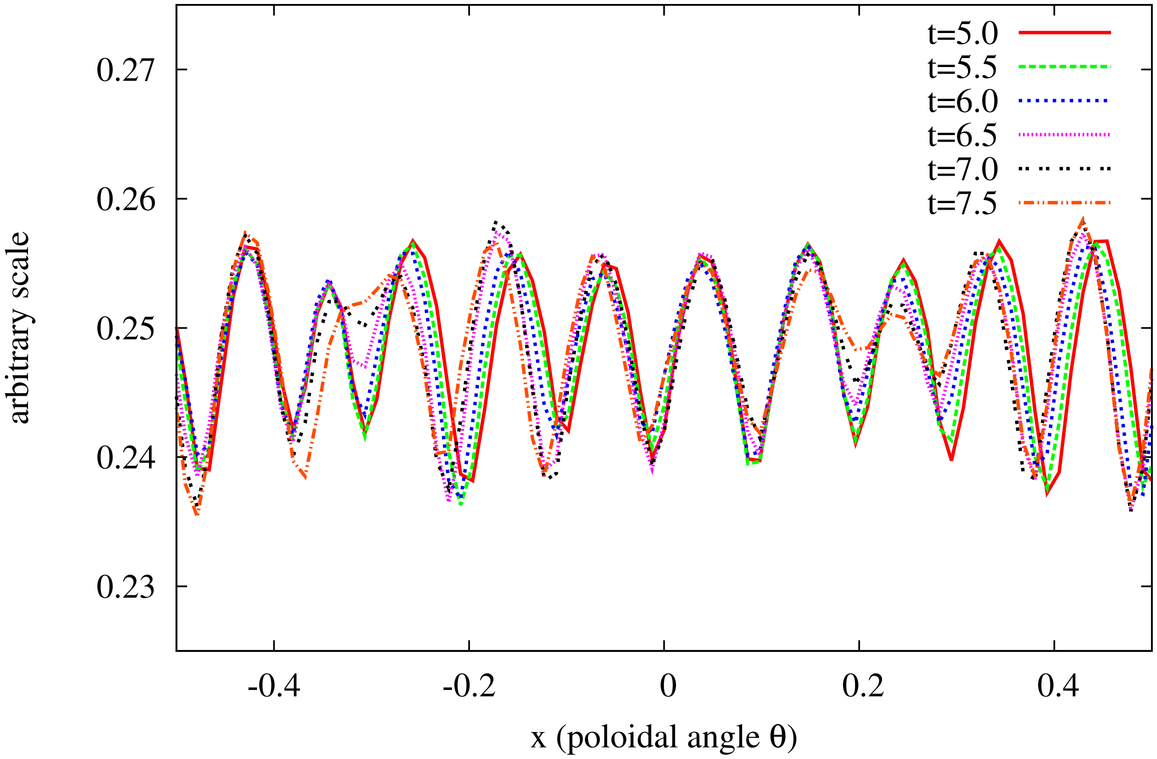
t=5.0
t=5.5
t=6.0
t=6.5
t=7.0
t=7.5
arbitrary scale
0.27
0.26
0.25
0.24
0.23
-0.4
-0.2
0
0.2
0.4
x (poloidal angle θ)

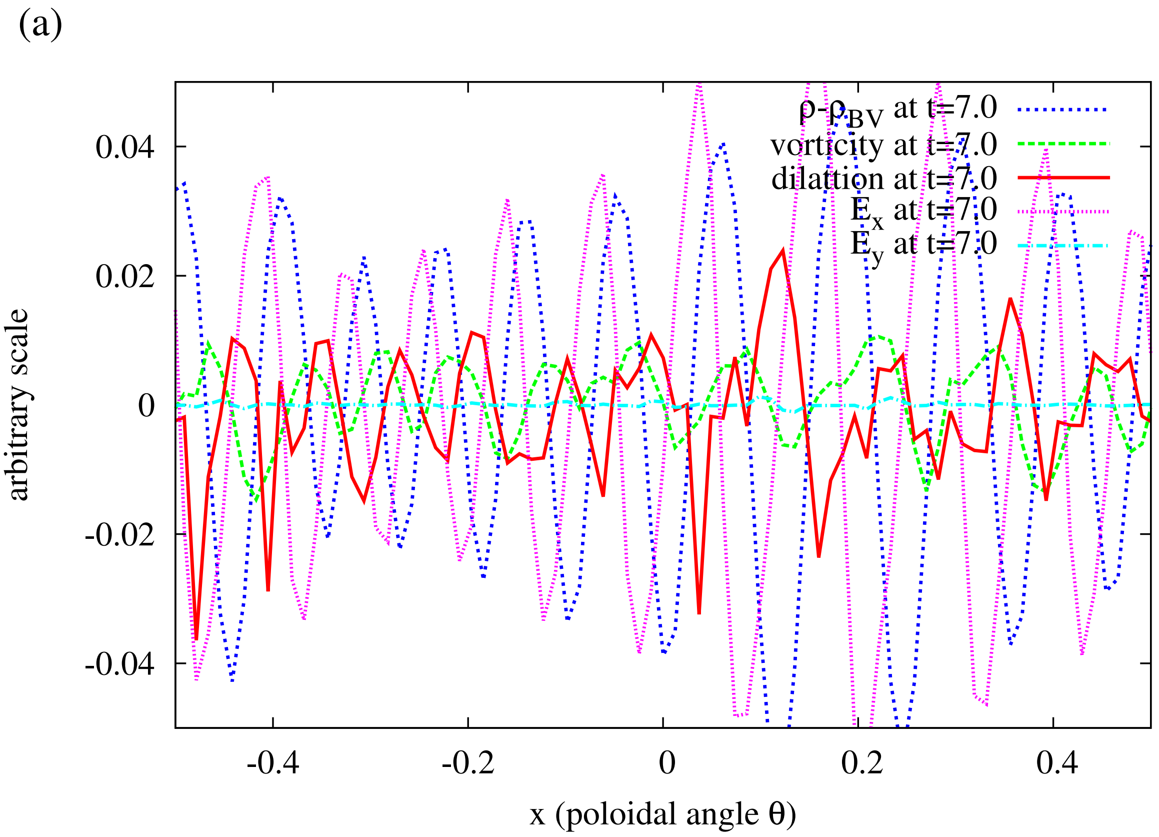
(a)
ρ-ρ_BV at t=7.0
vorticity at t=7.0
dilattion at t=7.0
E_x at t=7.0
E_y at t=7.0
arbitrary scale
0.04
0.02
0
-0.02
-0.04
-0.4
-0.2
0
0.2
0.4
x (poloidal angle θ)

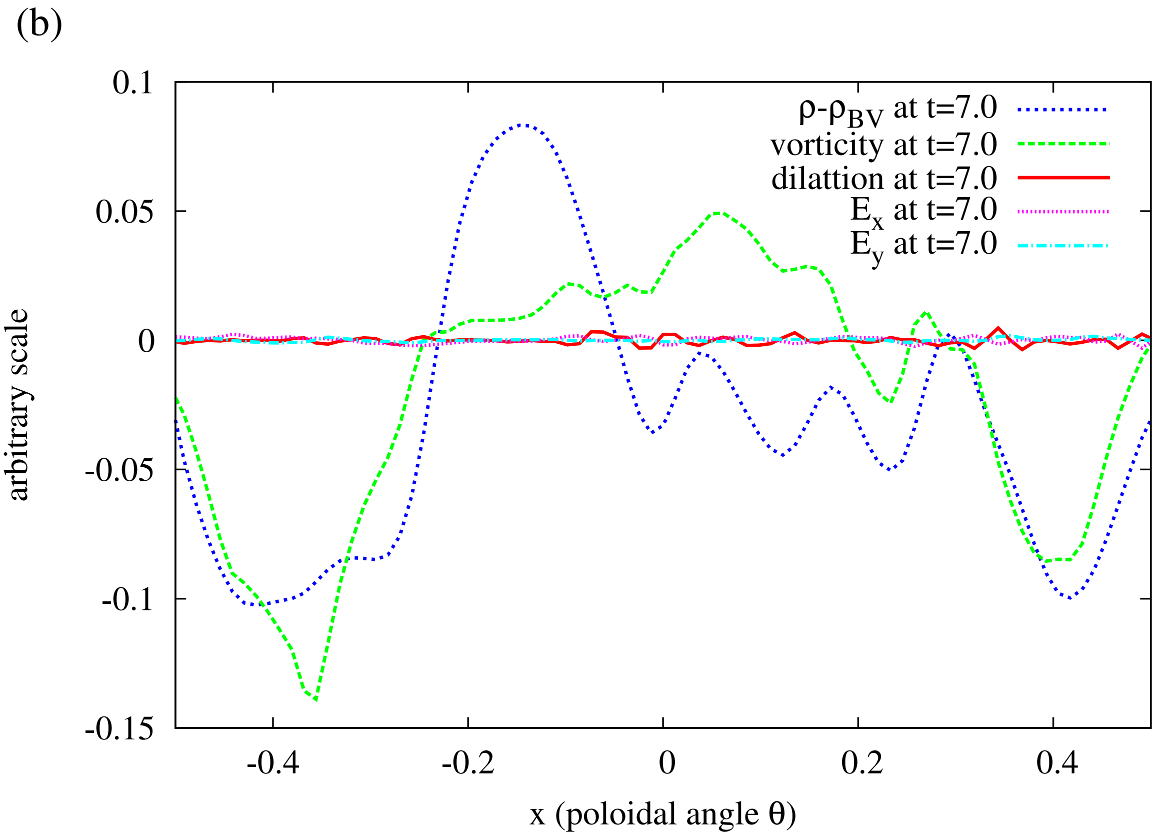
(b)
0.1
0.05
0
-0.05
-0.1
-0.15
-0.4
-0.2
0
0.2
0.4
arbitrary scale
x (poloidal angle θ)
ρ-ρ_{BV} at t=7.0
vorticity at t=7.0
dilattion at t=7.0
E_x at t=7.0
E_y at t=7.0

(c)

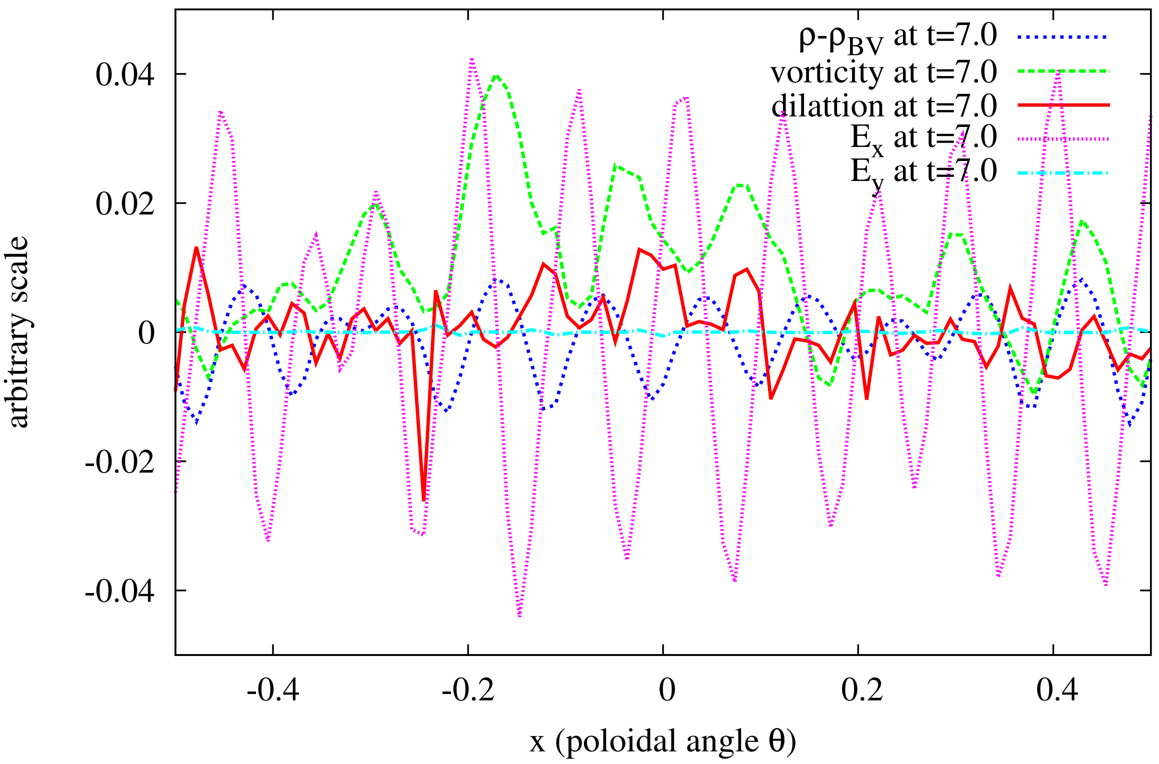
ρ-ρ_{BV} at t=7.0
vorticity at t=7.0
dilattion at t=7.0
E_x at t=7.0
E_y at t=7.0
arbitrary scale
0.04
0.02
0
-0.02
-0.04
-0.4
-0.2
0
0.2
0.4
x (poloidal angle θ)

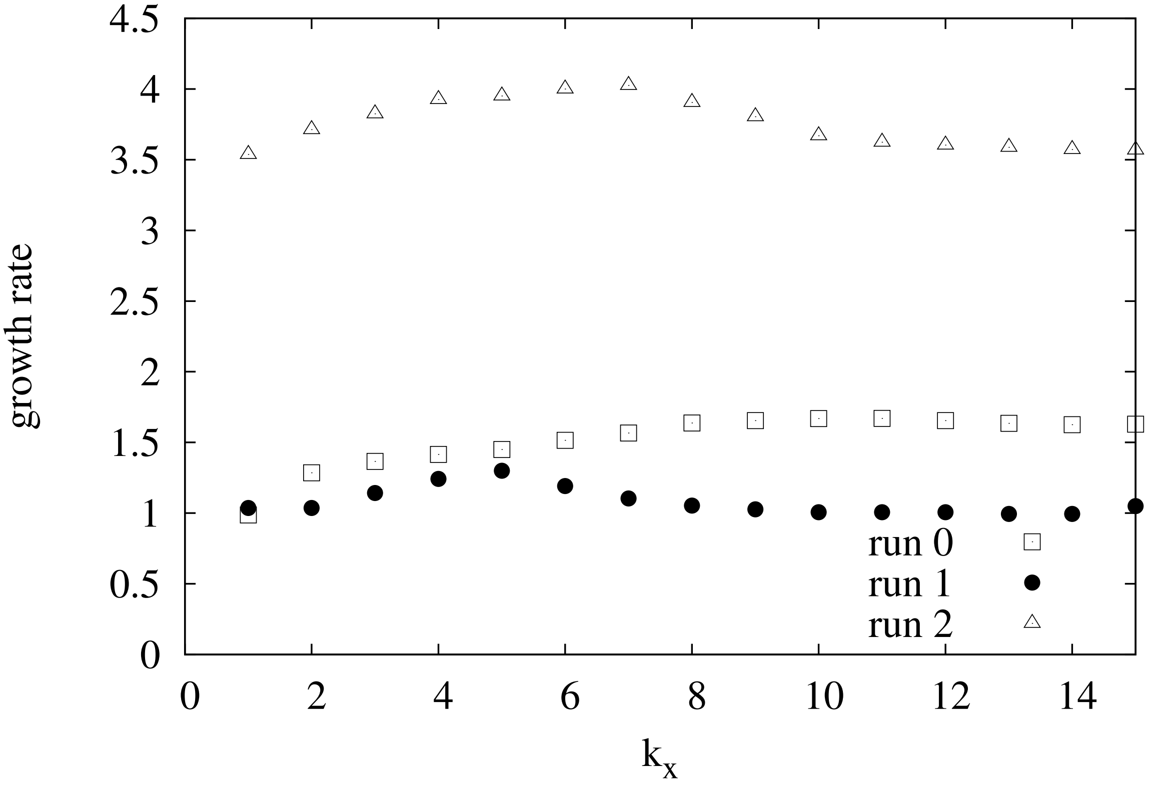
growth rate
4.5
4
3.5
3
2.5
2
1.5
1
0.5
0
0
2
4
6
8
10
12
14
k_x
run 0 □
run 1 ●
run 2 △

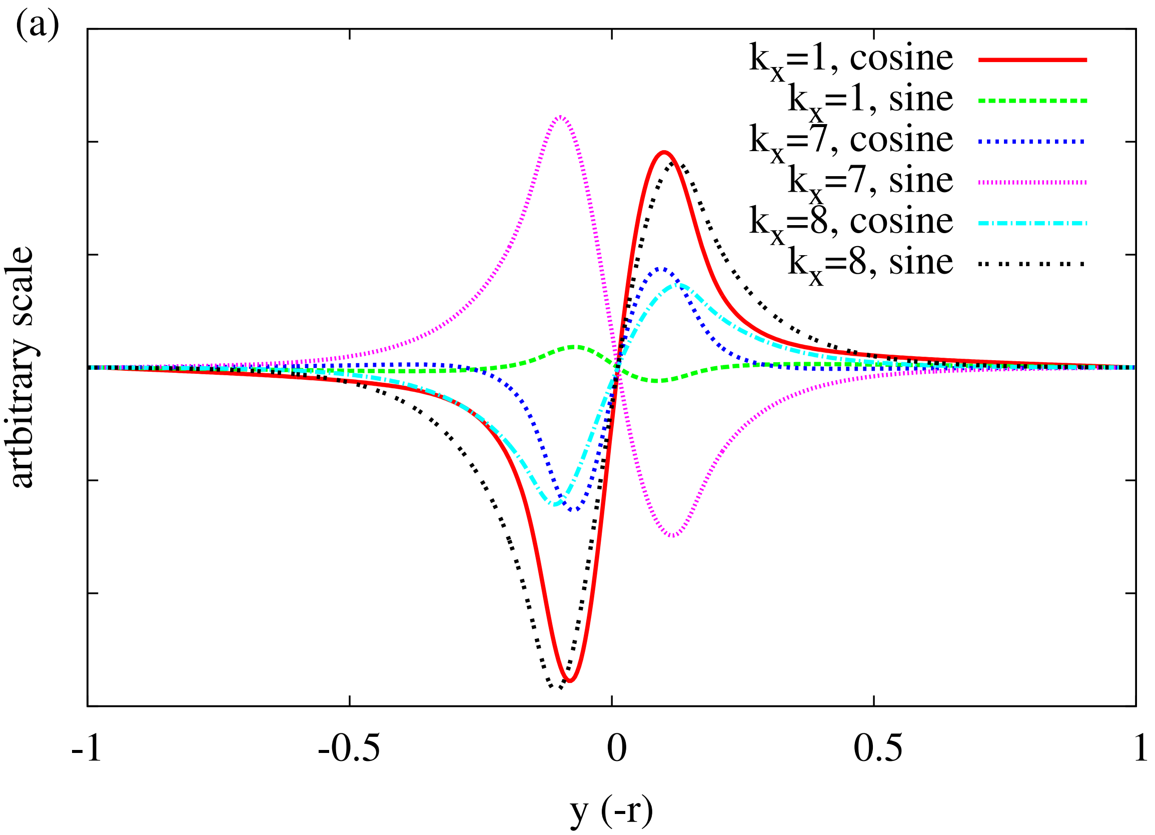
(a)
k_x=1, cosine
k_x=1, sine
k_x=7, cosine
k_x=7, sine
k_x=8, cosine
k_x=8, sine
artbitrary scale
-1
-0.5
0
0.5
1
y (-r)

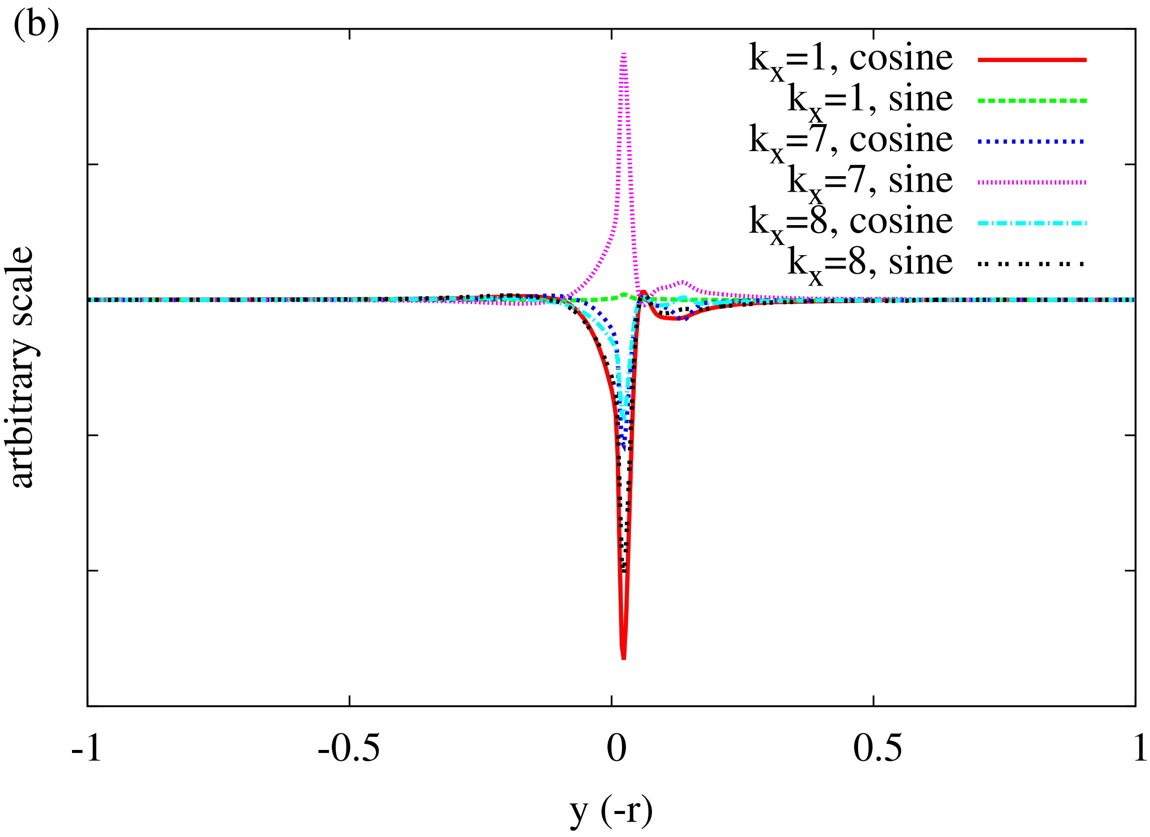
(b)
k_x=1, cosine
k_x=1, sine
k_x=7, cosine
k_x=7, sine
k_x=8, cosine
k_x=8, sine
artbitrary scale
-1
-0.5
0
0.5
1
y (-r)

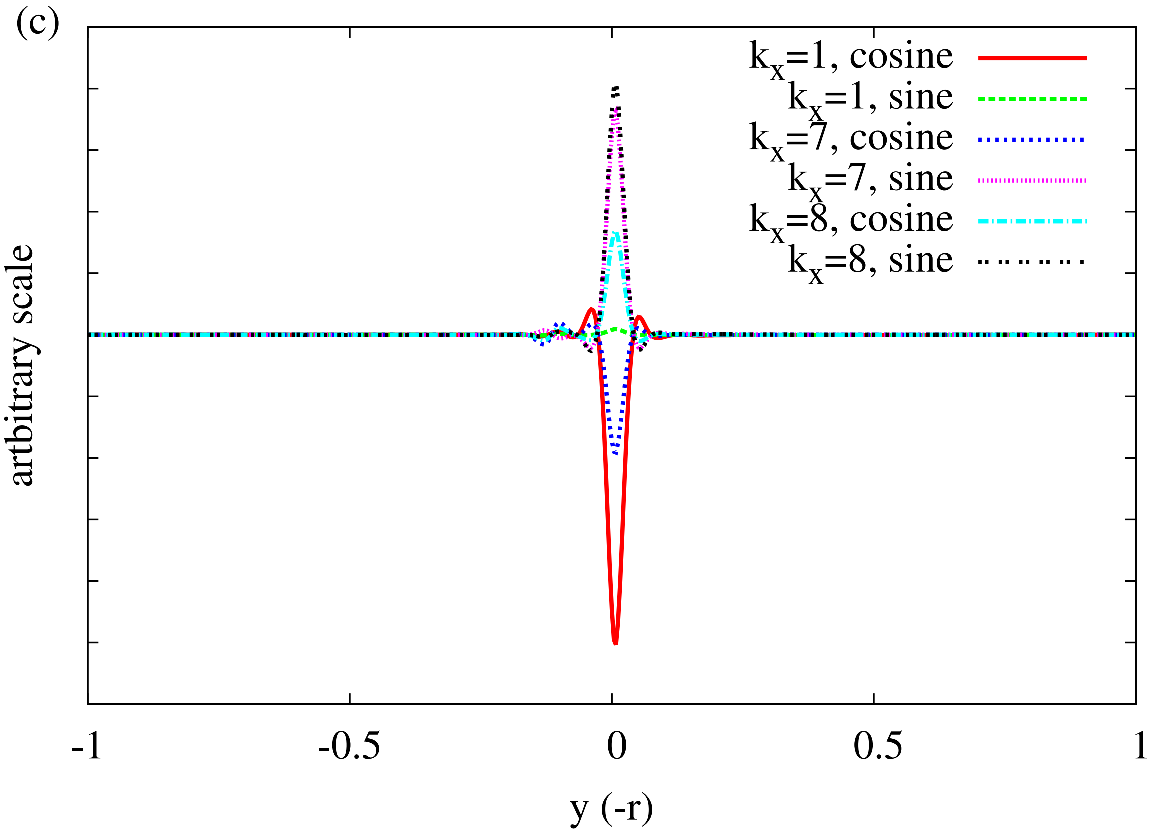
(c)
k_x=1, cosine
k_x=1, sine
k_x=7, cosine
k_x=7, sine
k_x=8, cosine
k_x=8, sine
artbitrary scale
-1
-0.5
0
0.5
1
y (-r)